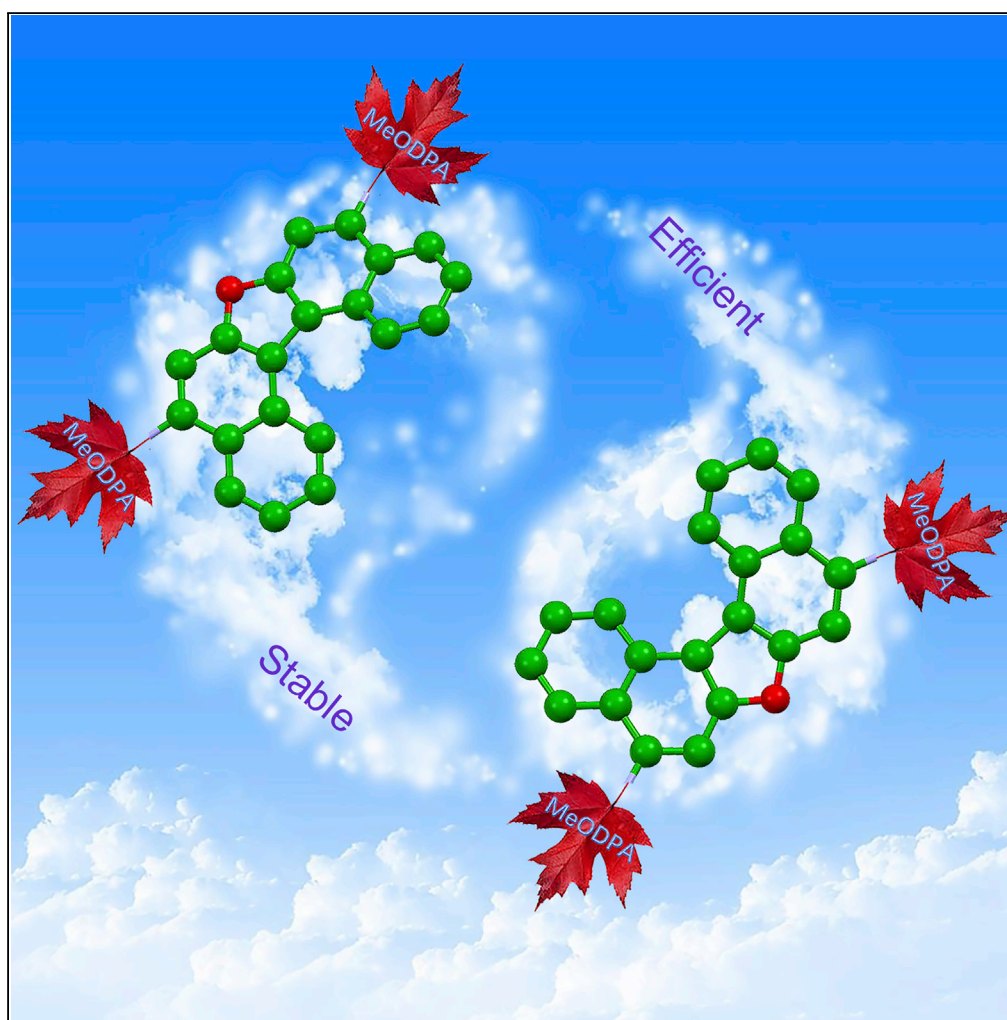**Article**

An Oxa[5]helicene-Based Racemic Semiconducting Glassy Film for Photothermally Stable Perovskite Solar Cells

Niansheng Xu, Yang Li, Damiano Ricciarelli, ..., Shaik M. Zakeeruddin, Michael Grätzel, Peng Wang

filippo@thch.unipg.it (F.D.A.)
pw2015@zju.edu.cn (P.W.)

HIGHLIGHTS

An oxa[5]helicene-based glassy semiconducting film with high hole mobility

A racemic organic thin film with improved phase stability under thermal stress

A 21% efficiency perovskite solar cell with excellent durability at 60°C under light

Article

An Oxa[5]helicene-Based Racemic Semiconducting Glassy Film for Photothermally Stable Perovskite Solar Cells

Niansheng Xu,[1] Yang Li,[1,2] Damiano Ricciarelli,[3,4] Jianan Wang,[1] Edoardo Mosconi,[3] Yi Yuan,[1] Filippo De Angelis,[3,4,5,*] Shaik M. Zakeeruddin,[2] Michael Grätzel,[2] and Peng Wang[1,6,*]

SUMMARY

Attaining the durability of high-efficiency perovskite solar cells (PSCs) operated under concomitant light and thermal stresses is still a serious concern before large-scale application. It is crucial to maintain the phase stability of the organic hole-transporting layer for thermostable PSCs across a range of temperatures sampled during device operation. To address this issue, we propose a racemic semiconducting glassy film with remarkable morphological stability, exemplified here by a low-molecular symmetry oxa[5]helicene-centered organic semiconductor (O5H-OMeDPA). The helical configuration of O5H-OMeDPA confers the trait of multiple-dimension charge transfer to the solid, resulting in high hole mobility of 6.7×10^{-4} cm^2 V^{-1} s^{-1} of a solution-processed glassy film. O5H-OMeDPA is combined with a triple-cation dual-halide lead perovskite to fabricate PSCs with power conversion efficiencies of 21.03%, outperforming the control cells with spiro-OMeTAD (20.44%). Moreover, the cells using O5H-OMeDPA exhibit good long-term stability during full-sunlight soaking at 60°C.

INTRODUCTION

Metal halide perovskite solar cells (PSCs) have stirred up intense research passions thanks to the steeply increasing power conversion efficiency (PCE) and cost-effective fabrication (Kojima et al., 2009; Kim et al., 2012; Burschka et al., 2013; Liu et al., 2013; Jeon et al., 2015; Hou et al., 2017; Luo et al., 2018). In a classical PSC, a hole-transporting layer (HTL) plays pivotal roles in both hole transporting and electron blocking. Moreover, a uniform and dense HTL can avert the penetration of moisture and oxygen from outside, which affects the long-term stability of the device (Wang et al., 2018a). Hitherto, an enormous amount of organic hole transporters has been developed (Calió et al., 2016; Wang et al., 2016), only a few of which, however, present superior photovoltaic efficiencies over the state-of-the-art spiro-OMeTAD, with PCEs exceeding 20% (Zhang et al., 2017a, 2017b; Ge et al., 2018; Xu et al., 2017; Jeon et al., 2018; Saliba et al., 2016).

The spiro-OMeTAD-based PSCs undergo a severe PCE damping under a certain thermal stress (Domanski et al., 2018), which is essentially associated with the phase transition from the amorphous state to the crystalline state during device operation (Malinauskas et al., 2015; Zhao et al., 2017). The dynamic phase transition of the solution-processed spiro-OMeTAD film is imputed to the high molecular symmetry (D_{2d} point group (Wang et al., 2018b)). Meantime, large-scale application of spiro-OMeTAD will encounter the issues of complicated preparation and purification cost. To date few stable PSCs using small-molecule hole transporters have been reported under the compounded stress of light and heat. In 2018, a benzodi-pyrrole-based hole conductor was used for PSCs with 17.2% PCE and good stability at 35°C (Shang et al., 2018). Later, Lee and his co-workers engineered a fluorene-terminated hole conductor for PSCs, which could maintain high stability at 60°C when stored in the dark (Jeon et al., 2018). Recently, Lin et al. designed three azahelicene derivatives as hole conductors for PSCs, among which the SY1-based device shows a PCE of 17.34% and an excellent ambient stability (Lin et al., 2018). Also, two [7]helicene derivatives with stable open-shell singlet biradical ground states were demonstrated as effective surface modifiers of the inorganic nickel oxide HTL in PSCs (Lee et al., 2019).

In this study, we explore the possibility of using a racemic glassy organic film composed of enantiomers, for the phase stability control of the HTL in PSCs. As a proof of concept, we design a low-molecule-symmetry

[1]Department of Chemistry, Zhejiang University, Hangzhou 310028, China

[2]Laboratory of Photonics and Interfaces, Institute of Chemical Sciences & Engineering, École Polytechnique Fédérale de Lausanne, Lausanne 1015, Switzerland

[3]Department of Chemistry, Biology and Biotechnology, University of Perugia, Via Elce di Sotto 8, 06123 Perugia, Italy

[4]Computational Laboratory for Hybrid/Organic Photovoltaics, CNR-ISTM, Via Elce di Sotto 8, 06123 Perugia, Italy

[5]D3-Computation, Istituto Italiano di Tecnologia, Via Morego, Genova, Italy

[6]Lead Contact

*Correspondence:
filippo@thch.unipg.it (F.D.A.),
pw2015@zju.edu.cn (P.W.)
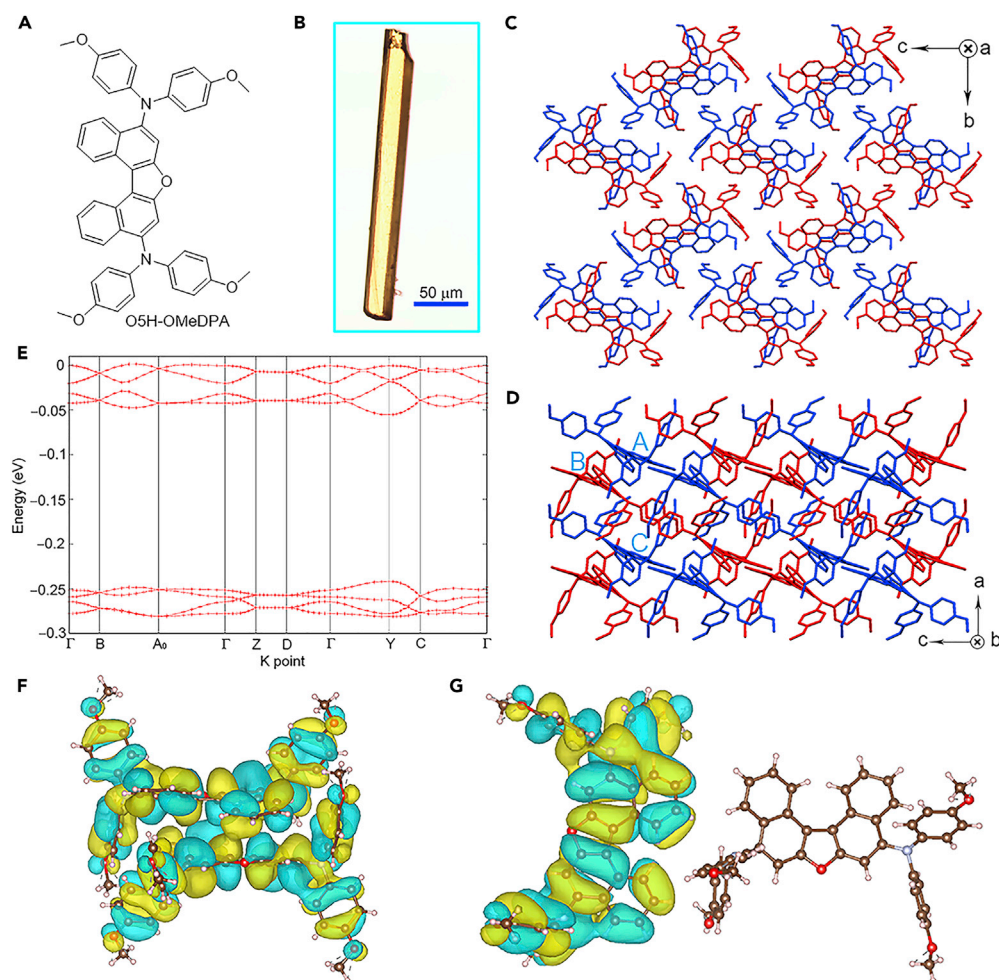
https://doi.org/10.1016/j.isci.2019.04.031

Figure 1. Molecular Structure, Molecular Packing, and Energy Band

(A) Chemical structure of O5H-OMeDPA.

(B) Optical microscopic image of an O5H-OMeDPA single crystal.

(C and D) Crystal structures along the *a* axis view (C) and the *b* axis view (D), with color-coded molecules: blue, enantiomer *P*; red, enantiomer *M*.

(E) DFT-calculated vcalence band structure of the O5H-OMeDPA single crystal. General gradient approximation (GGA) was used with the Perdew–Burke–Ernzerhof (PBE) functional to describe the exchange-correlation potential. In the band graphic, high-symmetry points in the first Brillouin zone are labeled in the crystallographic coordinates as follows: (Γ) (0,0,0), (B) (0,0,0.5), (A_0) (0.5,0.0,0.5), (Z) (0,0.5,0), (D) (0,0.5,0.5), (Y) (0.5,0,0), and (C) (0.5,0.5,0).

(F) HOMO of an *a*-laying dimer.

(G) HOMO of a *bc*-laying dimer.

helicene-based organic semiconductor, N^5,N^5,N^9,N^9-tetrakis(4-methoxyphenyl)dinaphtho[2,1-*b*:1′,2′-*d*] furan-5,9- diamine (abbreviated as O5H-OMeDPA, Figure 1A). O5H-OMeDPA consists of an oxa-[5]helicene core and two electron-donating bis(4-methoxyphenyl)amine segments (Figure 1A). As reported in the literature (Nakahara et al., 2013), oxa-[5]helicene itself distorts with a 25° torsion angle of the two outer benzene rings in single crystal. The slight torsion configuration reduces the molecular symmetry (C_2 point group), which we think is beneficial for the formation of a glassy film. Also, the rigidity and twisting induced by the helical scaffold are considered to be favorable for the phase stability (Jhulki et al., 2016). Compared with the triangular pyramid configuration of spirobifluorene in spiro-OMeTAD, the relative planarity of helicene (Lin et al., 2018) may enhance the hole mobility. Our preliminary studies have shown that PSCs with O5H-OMeDPA as HTL present a high PCE of 21.03% and good stability under continuous full-sunlight soaking at 60°C.

RESULTS

Synthesis, Molecular Packing, and Hole Transportation

The synthesis sequence leading to O5H-OMeDPA started with the acid-catalyzed cyclization of 1,1′-binaphthalene-2,2′-diol, which is followed by bromination and Buchwald-Hartwig cross-coupling (Scheme S1). The synthesis resulted in a total yield of 80%. The overall material cost (Table S1) for 1 g O5H-OMeDPA in our laboratory is estimated to be less than one-tenth of that for spiro-OMeTAD (Ge et al., 2018), which makes large-scale synthesis and application viable. The molecular geometry optimization by density functional theory (DFT) method reveals that the oxa[5]helicene segment distorts with a torsion angle of 27.92° and the highest occupied molecular orbital (HOMO) of O5H-OMeDPA is delocalized over the whole π-conjugated skeleton, which is decisive for intermolecular hole hopping (Figure S1).

High-performance organic HTLs are always amorphous to ensure a complete coverage of the underlying perovskite in PSCs. The thin films are usually grown rapidly via spin-coating to prevent the formation of crystallites. However, the alignment of adjacent molecules in these films likely resembles that in the single crystal to some extent (Rivnay et al., 2012; Baldo et al., 2001). To elucidate the molecular packing and charge transport characteristics of O5H-OMeDPA in the solid state, we grew its single crystals by slowly evaporating a saturated, racemic solution of dichloromethane/heptane. The as-grown O5H-OMeDPA single crystals present an overall crack-free morphology and distinct borders (Figure 1B). X-ray crystallographic structure analysis was carried out to define the molecular packing (Figure S2 and Table S2). As displayed in Figures 1C and 1D, a pair of enantiomers M and P are observed in the crystal. As Figure S3 presents, the oxa[5]helicene segment distorts with a torsion angle of 30.89°, which is slightly larger than that of DFT-optimized geometry (Figure S1). For the O5H-OMeDPA geometry from single crystal, HOMO is also wholly delocalized over the electronic skeleton (Figure S3B). The enantiomers form an anti-parallel face-to-face dimer. The dimers stack on top of each other to form slipped columnar motifs along the a axis, via the C-H•••π interaction of the terminal methoxyphenyl with the oxa[5]helicene core. Within the crystallographic bc-plane the dimers arrange in T-shape herringbone pattern, and their cohesion is achieved by London dispersion forces.

The electronic band structure of the O5H-OMeDPA crystal was calculated by DFT to gain insights on hole conductivity. From the results shown in Figures 1E and S4, one can notice that the band dispersion is quite small, as is typical of organic HTMs. Differences between adjacent energy levels show variations within 0.02 eV, depending on the directions of reciprocal space (i.e., ΓZ, ΓB, and ΓY). We also computed hole effective masses and electron transfer integrals (Table S3). Along the ΓY direction of the Brillouin zone (the crystallographic a axis), we recorded an effective hole mass of 8.35 m_e. The values are smaller along the ΓZ and ΓB directions of the Brillouin zone, being 5.17 and 6.67 m_e, respectively, suggesting the higher hole mobilities along the b and c axes of the lattice space (see Figures 1C and 1D).

Now we turn to the dimers A-B and B-C along the crystallographic a axis in Figure 1D. The calculated transfer integrals (Table S3) are 41.12 meV for dimer A-B (path 5 in Figure S5) and 1.32 meV for dimer B-C (path 6 in Figure S5). As Figure 1F shows, the HOMO of dimer A-B is fully extended on both A and B due to the strong electron coupling. However, the hole mobility along the a axis is not high, actually limited by the weak coupling region (B-C), which compensates the benefit of strong π-π interaction in dimer A-B. The transfer integral of path 2 and 4 (Figure S5) is 6.27 meV, contributing to a valid hole conduction in the bc plane, although the intermolecular electron coupling is not very strong (Figure 1G). The single crystal hole mobility of O5H-OMeDPA was theoretically calculated by using the Einstein relation $\mu = eD/k_BT$ based on the hopping model (Nguyen et al., 2015), and the calculated hole mobility reaches up to 4.7×10^{-2} cm^2 V^{-1} s^{-1} (Figure S5 and Table S3).

The hole-transporting property of the O5H-OMeDPA films spun from chlorobenzene was investigated by measuring the space-charge limited currents of hole-only devices. The average hole mobility of a non-doped O5H-OMeDPA film is 3.3×10^{-5} cm^2 V^{-1} s^{-1} (Figure 2A), over five times higher than that of 5.0×10^{-6} cm^2 V^{-1} s^{-1} for the spiro-OMeTAD control, suggesting the merit of multiple-dimensional charge transfer pathways in a semiconducting glassy film. With lithium bis(trifluoromethylsulfonyl)imide (LiTFSI) and 4-*tert*-butylpyridine (TBP) as additives, the hole mobility of the spin-coated O5H-OMeDPA film was remarkably improved to 6.7×10^{-4} cm^2 V^{-1} s^{-1} (Figure 2A), which is about three times higher than that of 2.1×10^{-4} cm^2 V^{-1} s^{-1} for the spiro-OMeTAD counterpart.
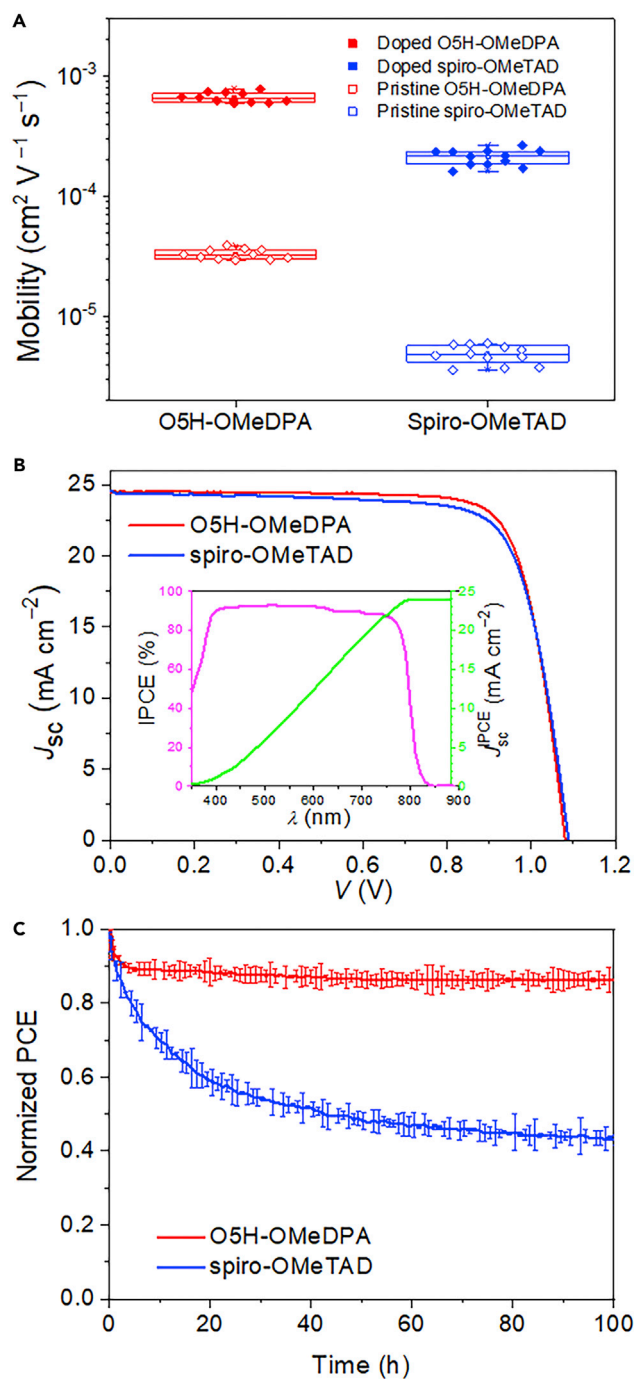
Figure 2. Conductivity, Photovoltaic Characterization, and Photothermal Stability

(A) Space-charge limited currents hole mobilities of O5H-OMeDPA and spiro-OMeTAD spin coated on the substrate of poly(3,4-ethylenedioxythiophene) polystyrene sulfonate.

(B) J-V characteristic (reverse scan) of a champion PSC with O5H-OMeDPA as the hole-transporting layer measured under 100 mW cm^{-2}, AM 1.5G illumination. The data for a control cell with spiro-OMeTAD are also included. The inset is the IPCE spectrum and integrated J_{SC} from the IPCE curve for the O5H-OMeDPA based cell.

(C) Normalized PCEs of unencapsulated devices examined via MPP tracking under the continuous AM1.5 G equivalent light irradiation and nitrogen flow at 60°C. Error bars refer to the average deviations of four cells.

HTL	Light Intensity [mW cm^{-2}]	$J_{SC}^{IPCE\ a}$ [mA cm^{-2}]	J_{SC}[mA cm^{-2}]	V_{OC}[V]	FF	PCE[%]
O5H-OMeDPA	99.0	23.76	24.48	1.081	0.788	21.03
Spiro-OMeTAD	99.1	23.85	24.53	1.089	0.757	20.44

Table 1. Photovoltaic Parameters of Champion PSCs Measured under an Irradiance of 100 mW cm^{-2}, Simulated AM1.5G Sunlight

[a] J_{SC}^{IPCE} was derived with wavelength integration of the product of the measured IPCEs at the short-circuit and the standard AM1.5G emission spectrum (ASTM G173-03).

Device Efficiency and Stability

We adopted a triple cation perovskite, $(FAPbI_3)_{0.85}(MAPbBr_3)_{0.10}(CsPbI_3)_{0.05}(PbI_2)_{0.03}$, as the photoactive layer to fabricate PSCs on fluorine-doped tin oxide (FTO) substrates, based on the device structure: FTO/c-mp TiO$_2$/perovskite/HTL/Au. In Figure 2B, we present the current density-voltage (J-V) curves for the champion cells, and the extracted photovoltaic parameters are tabulated in Table 1. The PCE of the O5H-OMeDPA-based cell reaches 21.03%, with a short-circuit current (J_{SC}) of 24.48 mA cm^{-2}, an open-circuit voltage (V_{OC}) of 1.081 mV, and a fill factor (FF) of 0.788, outperforming the best spiro-OMeTAD control with a PCE of 20.44%. Furthermore, the maximum power point (MPP) tracking under AM 1.5G illumination (Figure S6) was conducted, affording a steady-state PCE of 20.03%. The hystrese of the corresponding cells were shown in Figure S7. The incident photon-to-electron conversion efficiency (IPCE) spectra of the cells are presented in the inset of Figure 2B. The O5H-OMeDPA cell achieves an integrated current density of 23.76 mA cm^{-2}, which is in close agreement with the J-V scan. A good reproducibility can be perceived from the narrow cell parameter distributions of 10 devices (Figure S8).

The operational stability tests were conducted by keeping PSCs at 60°C under 1 sun equivalent white-light-emitting diode (LED) illumination at MPP. After 100 h, the O5H-OMeDPA cell retains 86% of the initial PCE (Figure 2C). After the rapid initial burn-in decay, which is possibly caused by the migration of A-site cations of perovskite (Christians et al., 2018), the PCE remains practically stable. In contrast, the spiro-OMeTAD control has an over 40% loss in the initial PCE after 20 h (Figure 2C). The unstable behavior of spiro-OMeTAD is in agreement with the previous report (Domanski et al., 2018).

Film Morphology, Energy Level, and Hole Extraction

We performed atomic force microscopic (AFM) measurements to inspect the film morphology. The O5H-OMeDPA film deposited on the poly(3,4-ethylenedioxythiophene) polystyrene sulfonate substrate owns a smooth surface with a root mean square deviation of 0.39 nm (Figure S9). When being coated on the perovskite layer with LiTFSI and TBP as additives, the O5H-OMeDPA film still retains a continuous surface with full surface coverage (Figure 3A). By contrast, the spiro-OMeTAD control presents plenty of pinholes (the dark region in Figure 3B, marked with a red circle) and LiTFSI aggregates (the light region, marked with a green circle), in line with previous reports (Wang et al., 2018b).

To have a better understanding on the energy level alignment of O5H-OMeDPA with respect to the perovskite, UV photoelectron spectroscopy measurement was performed for the spin-coated thin films on an FTO glass. From the onset (E_i) and cutoff (E_{cutoff}) energy regions shown in Figure S10, we derived the HOMO energy level of solid O5H-OMeDPA, being −5.29 eV, which is 0.16 eV lower than −5.13 eV for spiro-OMeTAD. Compared with the bare perovskite film, photoluminescence (PL) was strongly quenched for the O5H-OMeDPA-coated sample, with a PL quenching (hole extraction) yield of 97.0% (Figure 3C), which is almost the same as the sample with spiro-OMeTAD (96.3%). The pristine perovskite film presents a long PL lifetime of 1.99 μs. The PL lifetime of an O5H-OMeDPA-coated perovskite film is reduced to 33.8 ns (Figure 3D), slightly shorter than that of the spiro-OMeTAD control (58.1 ns). Given the smaller driving force, the faster kinetics and higher yield of hole extraction suggest a stronger electronic coupling of O5H-OMeDPA with the perovskite than spiro-OMeTAD.

DISCUSSION

To gain further insight into the interface interaction between the newly synthesized HTM and the perovskite surface, the binding energy (ΔE_b) between O5H-OMeDPA and a modeled MAPbI$_3$ perovskite slab
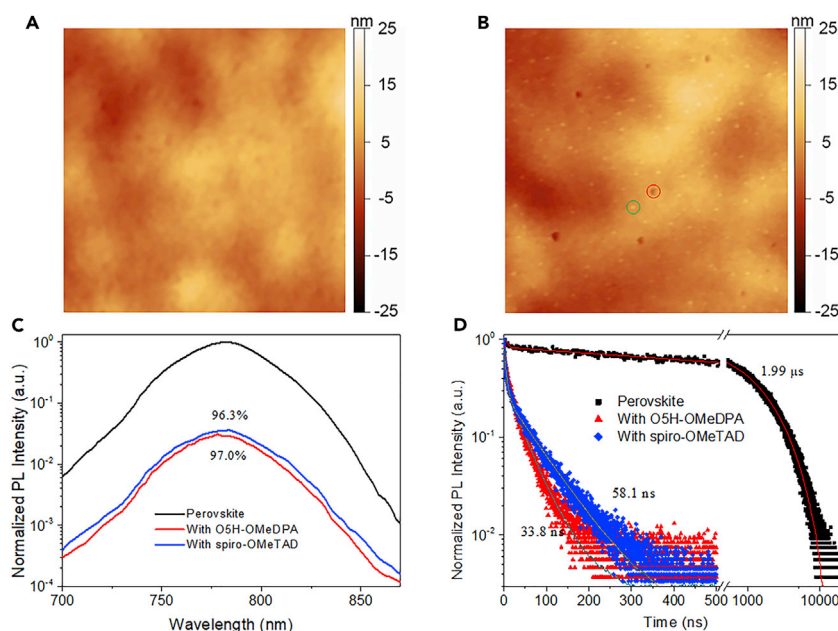
Figure 3. Surface Morphology and Hole Extraction

(A and B) AFM images (1 μm × 1 μm) of O5H-OMeDPA (A) and spiro-OMeTAD (B) spin coated on the substrates of perovskite. Note that the hole-transporting films are doped with LiTFSI and TBP.

(C and D) Steady-state photoluminescence (PL) spectra (C) and time-resolved PL traces (D) of a pristine perovskite film deposited on a mesoporous alumina film and the counterpart covered with O5H-OMeDPA or spiro-OMeTAD.

(Figure 4A) was computed by DFT, see Supplemental Information for details. The obtained value (ΔE_b) is −0.83 eV, which is significantly larger than that calculated for spiro-OMeTAD (−0.11 eV, Figure 4B). This study has unveiled the greater interfacial affinity of O5H-OMeDPA with perovskite, resulting in efficient hole extraction and higher interface stability. The isodensity plots in Figure 4C of valence band edge associated with the perovskite/O5H-OMeDPA confirm the large electronic coupling between the HTM and the perovskite, showing that the HOMO orbital of O5H-OMeDPA expands toward the MAPbI$_3$ slab. Furthermore, the HOMO energy is perfectly aligned with the perovskite valence band as suggested by the projected density of states diagrams in Figure 4D.

The growth of large crystalline domains in the HTL with a thickness of a few tens of nanometers has been suggested as one of the degradation causes of PSCs at elevated temperatures (Malinauskas et al., 2015). Therefore we investigated the influence of continuous thermal stress on the microstructure of solution-deposited glassy films with the aid of X-ray diffraction analysis. As depicted in Figures 4E and 4F, the as-deposited thin films are amorphous for both O5H-OMeDPA and spiro-OMeTAD. Circular dichroism spectrum has proved the racemic feature of the solution-processed O5H-OMeDPA film. After 12-h heating at 60°C, the O5H-OMeDPA film maintains the amorphous characteristic, whereas the spiro-OMeTAD control evolves into a crystalline film verified by the occurrence of multiple X-ray diffraction (XRD) peaks. The crystalline phase of the annealed spiro-OMeTAD thin film matches well with the single-crystal structure reported by Shi et al. (Shi et al., 2016). During crystallization, molecules in the thin film will move, forming closely packed phases and cracks simultaneously. The heat-induced phase transition is likely to deteriorate the interfacial contacts, impacting the hole extraction and transportation behaviors. Also, the change in film morphology will weaken the blocking effect of the HTL on Au diffusion into the perovskite layer, which severely affects the device performance under working conditions (Domanski et al., 2016). In recent years, certain interface materials have been used to suppress metal diffusion (Hou et al., 2017; Chen et al., 2017; Christians et al., 2018; Wu et al., 2019), which is a promising approach to further improve the stability of O5H-OMeDPA-based devices. It is also reported that additives can accelerate the crystallization of spiro-OMeTAD (Zhao et al., 2017). Hence, we also compared the morphologies and XRD patterns of the doped O5H-OMeDPA films before and after thermal aging at 60°C. No remarkable change upon aging was observed from AFM images (Figure S13). Also, the 60°C aged film is still amorphous (Figure S14).
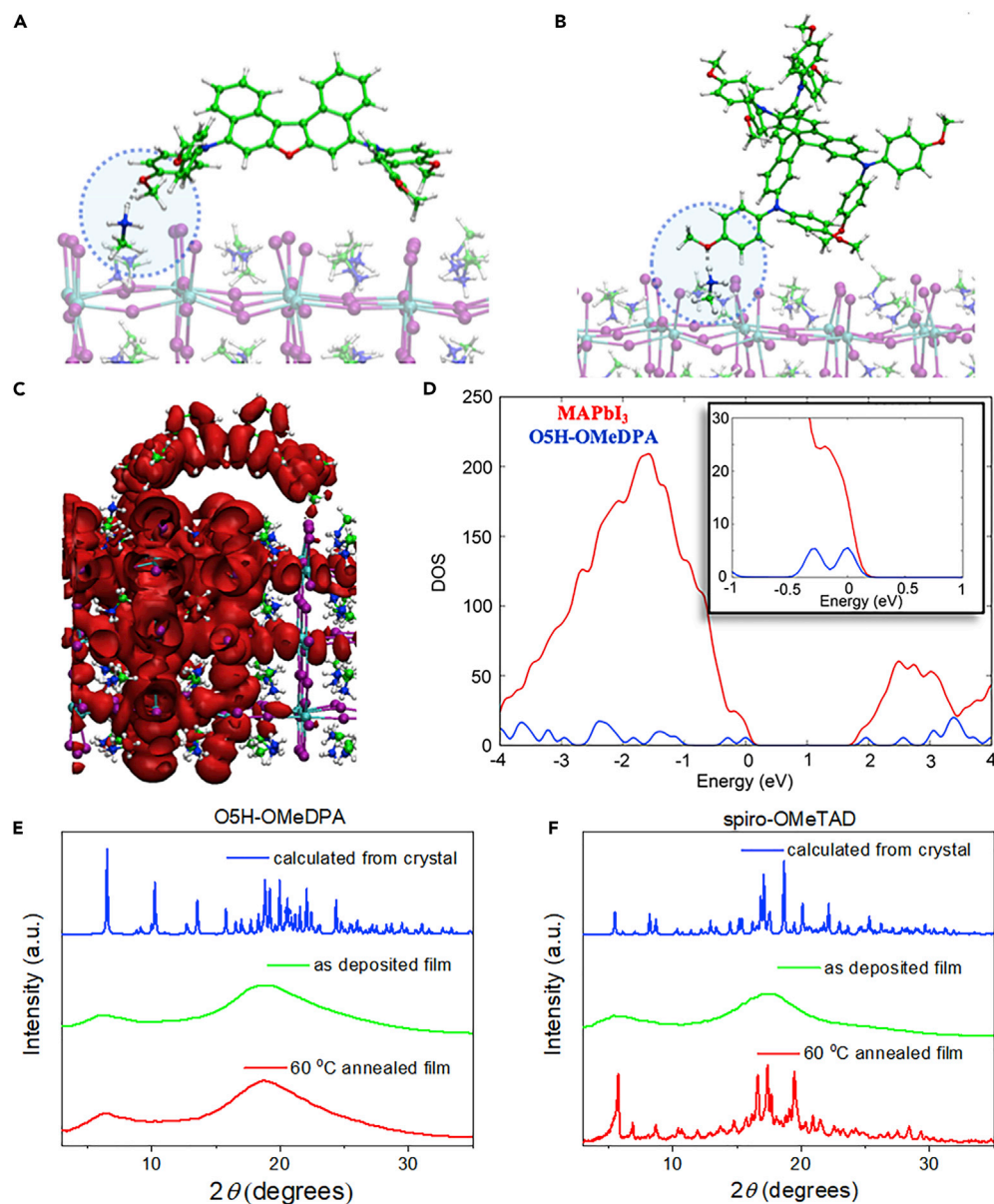
Figure 4. Interface Interaction and Phase Stability

(A and B) Optimized geometries of O5H-OMeDPA (A) and spiro-OMeTAD (B) interacting with a MAPbI$_3$ perovskite slab.

(C) Three-dimensional representation of valence band edge associated with the perovskite/O5H-OMeDPA interface.

(D) Projected density of states of O5H-OMeDPA molecule adsorbed on the (110) surface of MAPbI$_3$.

(E and F) Comparison of experimental XRD patterns of the as-deposited films and the films aged at 60°C for 12 h with the calculated XRD patterns based on single-crystal parameters: O5H-OMeDPA (E) and spiro-OMeTAD (F).

Overall, the superior photo- and thermal stability of the O5H-OMeDPA-based PSCs demonstrated here highlights the grand potential of a racemic semiconducting glassy film of helicenes for organic opto-electronic devices.

Limitations of the Study

To validate the industrial pass-fail qualification tests IEC61215, the thermal stability of our PSCs was also evaluated at 85°C in the dark. The device degraded rapidly, which is likely associated with the crystallization of an amorphous O5H-OMeDPA film at 85°C (Figure S14), apart from the instability of the perovskite

layer itself. This highlights the future need of developing new materials that can tolerate higher thermal stress.

METHODS

All methods can be found in the accompanying Transparent Methods supplemental file.

SUPPLEMENTAL INFORMATION

Supplemental Information can be found online at https://doi.org/10.1016/j.isci.2019.04.031.

AUTHOR CONTRIBUTIONS

P.W. conceived the idea and directed the research. N.X. and J.W. synthesized hole transporter; performed the UPS, AFM, and XRD measurements; and carried out some preliminary photovoltaic evaluation. Y.L. fabricated solar cells and conducted the photovoltaic characterization. D.R. and E.M. calculated the band structure and binding energy. N.X., Y.L., D.R., F.D.A., and P.W. analyzed the data, assembled the plots, and prepared the manuscript. Y.Y., S.M.Z., and M.G. revised the manuscript.

DECLARATION OF INTERESTS

The authors declare no competing interests.

REFERENCES

Baldo, M.A., Soos, Z.G., and Forrest, S.R. (2001). Local order in amorphous organic molecular thin films. Chem. Phys. Lett. *347*, 297–303.

Burschka, J., Pellet, N., Moon, S.-J., Humphry-Baker, R., Gao, P., Nazeeruddin, M.K., and Grätzel, M. (2013). Sequential deposition as a route to high-performance perovskite-sensitized solar cells. Nature *499*, 316–320.

Calió, L., Kazim, S., Grätzel, M., and Ahmad, S. (2016). Hole-transport materials for perovskite solar cells. Angew. Chem. Int. Ed. *55*, 14522–14545.

Chen, C., Zhang, S., Wu, S., Zhang, W., Zhu, H., Xiong, Z., Zhang, Y., and Chen, W. (2017). Effect of BCP buffer layer on eliminating charge accumulation for high performance of inverted perovskite solar cells. RSC Adv. *7*, 35819–35826.

Christians, J.A., Schulz, P., Tinkham, J.S., Schloemer, T.H., Harvey, S.P., Tremolet de Villers, B.J., Sellinger, A., Berry, J.J., and Luther, J.M. (2018). Tailored interfaces of unencapsulated perovskite solar cells for >1,000 hour operational stability. Nat. Energy *3*, 68–74.

Domanski, K., Correa-Baena, J.-P., Mine, N., Nazeeruddin, M.K., Abate, A., Saliba, M., Tress, W., Hagfeldt, A., and Grätzel, M. (2016). Not all that glitters is gold: metal-migration-induced degradation in perovskite solar cells. ACS Nano *10*, 6306–6314.

Domanski, K., Alharbi, E.A., Hagfeldt, A., Grätzel, M., and Tress, W. (2018). Systematic investigation of the impact of operation conditions on the degradation behaviour of perovskite solar cells. Nat. Energy *3*, 61–67.

Ge, Q.-Q., Shao, J.-Y., Ding, J., Deng, L.-Y., Zhou, W.-K., Chen, Y.-X., Ma, J.-Y., Wan, L.-J., Yao, J., Hu, J.-S., and Zhong, Y.-W. (2018). A two-dimensional hole-transporting material for high-performance perovskite solar cells with 20 % average efficiency. Angew. Chem. Int. Ed. *57*, 10959–10965.

Hou, Y., Du, X., Scheiner, S., McMeekin, D.P., Wang, Z., Li, N., Killian, M.S., Chen, H., Richter, M., Levchuk, I., et al. (2017). A generic interface to reduce the efficiency-stability-cost gap of perovskite solar cells. Science *358*, 1192–1197.

Jeon, N.J., Noh, J.H., Yang, W.S., Kim, Y.C., Ryu, S., Seo, J., and Seok, S.I. (2015). Compositional engineering of perovskite materials for high-performance solar cells. Nature *517*, 476–480.

Jeon, N.J., Na, H., Jung, E.H., Yang, T.-Y., Lee, Y.G., Kim, G., Shin, H.-W., Seok, S.I., Lee, J., and Seo, J. (2018). A fluorene-terminated hole-transporting material for highly efficient and stable perovskite solar cells. Nat. Energy *3*, 682–689.

Jhulki, S., Mishra, A.K., Chow, T.J., and Moorthy, J.N. (2016). Helicenes as all-in-one organic materials for application in OLEDs: synthesis and diverse applications of carbo- and aza[5]helical diamines. Chem. Eur. J. *22*, 9375–9386.

Kim, H.-S., Lee, C.-R., Im, J.-H., Lee, K.-B., Moehl, T., Marchioro, A., Moon, S.-J., Humphry-Baker, R., Yum, J.-H., Moser, J.E., et al. (2012). Lead iodide perovskite sensitized all-solid-state submicron thin film mesoscopic solar cell with efficiency exceeding 9%. Sci. Rep. *2*, 591.

Kojima, A., Teshima, K., Shirai, Y., and Miyasaka, T. (2009). Organometal halide perovskites as visible-light sensitizers for photovoltaic cells. J. Am. Chem. Soc. *131*, 6050–6051.

Lee, C.-C., Chen, C.-I., Fang, C.-T., Huang, P.-Y., Wu, Y.-T., and Chueh, C.-C. (2019). Improving performance of perovskite solar cells using [7] helicenes with stable partial biradical characters as the hole-extraction layers. Adv. Funct. Mater. *29*, 1808625.

Lin, Y.-S., Abate, S.Y., Lai, K.-W., Chu, C.-W., Lin, Y.-D., Tao, Y.-T., and Sun, S.-S. (2018). New helicene-type hole-transporting molecules for high-performance and durable perovskite solar cells. ACS Appl. Mater. Interfaces *10*, 41439–41449.

Liu, M., Johnston, M.B., and Snaith, H.J. (2013). Efficient planar heterojunction perovskite solar cells by vapour deposition. Nature *501*, 395–398.

Luo, D., Yang, W., Wang, Z., Sadhanala, A., Hu, Q., Su, R., Shivanna, R., Trindade, G.F., Watts, J.F., Xu, Z., et al. (2018). Enhanced photovoltage for inverted planar heterojunction perovskite solar cells. Science *360*, 1442–1446.

Malinauskas, T., Tomkute-Luksiene, D., Sens, R., Daskeviciene, M., Send, R., Wonneberger, H., Jankauskas, V., Bruder, I., and Getautis, V. (2015). Enhancing thermal stability and lifetime of solid-state dye-sensitized solar cells via molecular engineering of the hole-transporting material spiro-ometad. ACS Appl. Mater. Interfaces *7*, 11107–11116.

Nakahara, K., Mitsui, C., Okamoto, T., Yamagishi, M., Miwa, K., Sato, H., Yamano, A., Uemura, T., and Takeya, J. (2013). Single-crystal field-effect transistors with a furan-containing organic semiconductor having a twisted π-electronic system. Chem. Lett. *42*, 654–656.

Nguyen, T.P., Shim, J.H., and Lee, J.Y. (2015). Density functional theory studies of hole mobility in picene and pentacene crystals. J. Phys. Chem. C *119*, 11301–11310.

Rivnay, J., Mannsfeld, S.C.B., Miller, C.E., Salleo, A., and Toney, M.F. (2012). Quantitative determination of organic semiconductor microstructure from the molecular to device scale. Chem. Rev. *112*, 5488–5519.

Saliba, M., Orlandi, S., Matsui, T., Aghazada, S., Cavazzini, M., Correa-Baena, J.-P., Gao, P., Scopelliti, R., Mosconi, E., Dahmen, K.-H., et al. (2016). A molecularly engineered hole-transporting material for efficient perovskite solar cells. Nat. Energy *1*, 15017.

Shang, R., Zhou, Z., Nishioka, H., Halim, H., Furukawa, S., Takei, I., Ninomiya, N., and Nakamura, E. (2018). Disodium benzodipyrrole sulfonate as neutral hole-transporting materials for perovskite solar cells. J. Am. Chem. Soc. *140*, 5018–5022.

Shi, D., Qin, X., Li, Y., He, Y., Zhong, C., Pan, J., Dong, H., Xu, W., Li, T., Hu, W., et al. (2016). Spiro-OMeTAD single crystals: remarkably enhanced charge-carrier transport via mesoscale ordering. Sci. Adv. *2*, e1501491.

Wang, J., Liu, K., Ma, L., and Zhan, X. (2016). Triarylamine: versatile platform for organic, dye-sensitized, and perovskite solar cells. Chem. Rev. *116*, 14675–14725.

Wang, Y., Yue, Y., Yang, X., and Han, L. (2018a). Toward long-term stable and highly efficient perovskite solar cells via effective charge transporting materials. Adv. Energy Mater. *8*, 1800249.

Wang, X., Zhang, J., Yu, S., Yu, W., Fu, P., Liu, X., Tu, D., Guo, X., and Li, C. (2018b). Lowering molecular symmetry to improve the morphological properties of the hole-transport layer for stable perovskite solar cells. Angew. Chem. Int. Ed. *57*, 12529–12533.

Wu, S., Chen, R., Zhang, S., Babu, B.H., Yue, Y., Zhu, H., Yang, Z., Chen, C., Chen, W., Huang, Y., et al. (2019). A chemically inert bismuth interlayer enhances long-term stability of inverted perovskite solar cells. Nat. Commun. *10*, 1161.

Xu, B., Zhang, J., Hua, Y., Liu, P., Wang, L., Ruan, C., Li, Y., Boschloo, G., Johansson, E.M.J., Kloo, L., et al. (2017). Tailor-making low-cost spiro [fluorene-9,9'-xanthene]-based 3D oligomers for perovskite solar cells. Chem *2*, 676–687.

Zhang, J., Xu, B., Yang, L., Mingorance, A., Ruan, C., Hua, Y., Wang, L., Vlachopoulos, N., Lira-Cantú, M., Boschloo, G., et al. (2017a). Incorporation of counter ions in organic molecules: new strategy in developing dopant-free hole transport materials for efficient mixed-ion perovskite solar cells. Adv. Energy Mater. *7*, 1602736.

Zhang, F., Wang, Z., Zhu, H., Pellet, N., Luo, J., Yi, C., Liu, X., Liu, H., Wang, S., Li, X., et al. (2017b). Over 20% PCE perovskite solar cells with superior stability achieved by novel and low-cost hole-transporting materials. Nano Energy *41*, 469–475.

Zhao, X., Kim, H.-S., Seo, J.-Y., and Park, N.-G. (2017). Effect of selective contacts on the thermal stability of perovskite solar cells. ACS Appl. Mater. Interfaces *9*, 7148–7153.

Supplemental Information

An Oxa[5]helicene-Based Racemic

Semiconducting Glassy Film for Photothermally

**Stable Perovskite Solar Cells**

Niansheng Xu, Yang Li, Damiano Ricciarelli, Jianan Wang, Edoardo Mosconi, Yi Yuan, Filippo De Angelis, Shaik M. Zakeeruddin, Michael Grätzel, and Peng Wang

Supplemental Information

Transparent Methods

Materials. [1,1'-Binaphthalene]-2,2'-diol, *p*-toluenesulfonic acid, *N*-bromosuccinimide, 4,4'-dimethoxydiphenylamine, tris(dibenzylideneacetone)dipalladium (Pd$_2$(dba)$_3$), sodium *tert*-butoxide (NaO(*t*-Bu)), and tri-*tert*-butylphosphine tetrafluoroborate (P(*t*-Bu)$_3$·HBF$_4$) were purchased from Energy Chemical (Shanghai, China). Other chemicals were purchased and used without further purification. The three-step synthetic route to O5H-OMeDPA from [1,1'-binaphthalene]-2,2'-diol is shown in Scheme S1.

Scheme S1. Synthetic Route of O5H-OMeDPA
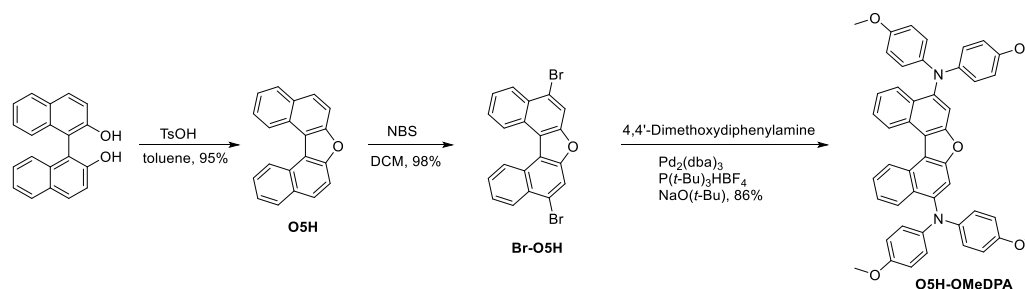
Dinaphtho[2,1-*b*:1',2'-*d*]furan (O5H [Areephong et al., 2004]) and 5,9-dibromodinaphtho[2,1-*b*:1',2'-*d*]furan (Br-O5H [Kunugi et al., 2014]) were synthesized according to the reported procedures in the yields of 95% and 98%, respectively, and identified by ^{1}H NMR spectra. N^5,N^5,N^9,N^9-tetrakis(4-methoxyphenyl)dinaphtho[2,1-*b*:1',2'-*d*]furan-5,9-diamine (O5H-OMeDPA) was prepared as follows: to a three-neck round bottom flask were added 5,9-dibromodinaphtho[2,1-*b*:1',2'-*d*]furan (852 mg, 2.00 mmol), 4,4′-dimethoxydiphenylamine (962 mg, 4.20 mmol), Pd$_2$(dba)$_3$ (91 mg, 0.10 mmol), P(*t*-Bu)$_3$·HBF$_4$ (58 mg, 0.20 mmol), NaO(*t*-Bu) (577 mg, 6.00 mmol), and toluene (50 mL). The reaction mixture was refluxed overnight under nitrogen. The mixture was filtered through a silica gel pad. The filtrate was concentrated and the residue was purified by column chromatography on alumina to afford a yellow solid, O5H-OMeDPA (1.24 g, 1.72 mmol) in 86% yield. ^{1}H NMR (400 MHz, THF-d_8) $δ$ = 9.15 (d, J = 8.5 Hz, 2H), 8.27 (dd, J = 8.5, 1.2

Hz, 2H), 7.68 (ddd, J = 8.3, 6.8, 1.3 Hz, 2H), 7.50 (s, 2H), 7.41 (ddd, J = 8.1, 6.9, 1.0 Hz, 2H), 6.99–6.91 (m, 8H), 6.82–6.74 (m, 8H), 3.71 ppm (s, 12H). ^{13}C NMR (101 MHz, THF-d_8) δ = 156.51, 155.96, 146.11, 143.85, 130.61, 129.78, 127.33, 127.26, 126.83, 125.51, 124.82, 117.97, 115.48, 112.97, 55.71 ppm. HR-MS (MALDI-TOF) m/z calcd. for ($C_{48}H_{38}N_2O_5$) [M]$^+$: 722.27752. Found: 722.27752. FT-IR (film) v_{max} = 3747, 3444, 2950, 2853, 1615, 1576, 1504, 1462, 1353, 1272, 1241, 1178, 1108, 1036, 828, 757, 714, 643, 597, 528 cm^{-1}.

UPS Measurements: The samples were spin-coated onto a fluorine-doped tin oxide (FTO) glass. UPS data were recorded on an ESCALAB 250Xi XPS System.

X-Ray Diffraction: Single crystal X-ray crystallographic data was collected on a Bruker D8 Venture (IµS 3.0) X-ray diffractometer, using graphite monochromatized Mo Kα (λ = 0.7107 Å) radiation. The APEX suite of programs and the SHELX suite of programs were used for data analysis. The structures were solved using direct methods and refined by full-matrix least-squares on F^2. Diagrams were prepared with Mercury 3.10. The crystallographic data are summarized in Table S2.

Band Structure Calculations: The calculations were carried out by using the Quantum Espresso program package (Giannozzi et al., 2009). The geometry was optimized starting from the experimentally measured x-ray structure employing the PBE functional (Perdew et al., 1996) and computing the SCF density at the Γ point (crystal coordinate 0.0, 0.0, 0.0) of the Brillouin-zone, using the experimental cell parameters reported in Table S1. Electron-ion interactions were described by the scalar relativistic ultrasoft pseudopotential, including the 2s and 2p states for O, N, and C, and the 1s one for H (Laasonen et al., 1991). Plane-wave basis set cutoffs for the smooth part of the wave functions and the augmented density of 25 and 200 Ry, respectively, were used. To obtain the band structure we chose the following paths in the reciprocal space (schematically reported in Figure S4): Γ–B–A$_0$–Γ–Z–D–Γ–Y–C–Γ. The energy eigenvalues were collected at each of the specified vertexes and at 8 different intermediate points laying on each segment of the path (i.e. 8 points for Γ–B, 8 points for B–A$_0$, and so on), using the electronic SCF density obtained at the Γ point.

Additionally, the density of states (DOS) were computed employing a 2×2×2 Monkhorst-Pack grid.

Mobility Calculation: The charge mobility can be calculated by Einstein relation

$$\mu = \frac{e}{k_B T} D,$$

where e is the electrical charge of a particle, D is the diffusion coefficient, k_B is the Boltzmann constant, and T is the Kelvin temperature. D can be expressed by the following approximate equation

$$D = \frac{1}{2n} \sum_i d_i^2 k_i p_i,$$

where n is the three dimensionalities of the single crystal, d_i represents the center-of-mass distance, k_i is the hopping rate, and p_i is the relative probability of the i path obtained by the equation

$$p_i = \frac{k_i}{\sum_i k_i}.$$

The hopping model is suitable for describing the charge transfer properties of organic compounds. The hopping rate (k_i) between the adjacent molecules according to the Marcus–Hush theory can be described as

$$k_i = \frac{V^2}{h} \left(\frac{\pi}{\lambda k_b T} \right)^{1/2} \exp\left(-\frac{\lambda}{4 k_b T} \right),$$

where h denotes the Planck constant, λ is the reorganization energy, and V is the transfer integral. The mobility is mainly related to charge transfer distance (d_i), the reorganization (λ), and the transfer integral. The reorganization energy is composed of two parts, inner reorganization energy and external reorganization energy. The small external reorganization energy can be ignored, and the inner reorganization energy can be estimated by the adiabatic potential energy surface approach

$$\lambda = \lambda_1 + \lambda_2 = (E_0^* - E_0) + (E_+^* - E_+),$$

here E_0 and E_+ are the energy of neutral molecule and the energy of cation, E_0^* and E_+^* are the energy of cation in neutral molecule geometry, and the energy of neutral molecule in cationic geometry. The transfer integral (V) can be estimated by the direct approach

3 / 30

$$V = <\psi_i^{\text{HOMO/LUMO}} \,|\, F \,|\, \psi_f^{\text{HOMO/LUMO}} >,$$

where ψ represents the HOMO/LUMO orbitals and F is the Fock operator for the dimer. M06-2X/6-31G(d,p) was employed for the transfer integral calculation.

Binding Energy Calculations: We computed the binding energies of the O5H-OMeDPA and Spiro-OMeTAD molecules with a perovskite slab employing the SIESTA 4.1 program package (Soler et al., 2002). Geometry optimizations were carried out at the PBE-GGA level using a DZ basis set along with non-relativistic pseudo-potentials for Pb, I, O, C, N, and H atoms. Pb atoms were treated with the WC-GGA (Wu and Cohen, 2006) relativistic pseudopotential. Electrons from O, C, and N 2s, 2p; H 1s; I 5s, 5p; Pb 6s, 6p, 5d shells were explicitly included in the calculations. Spin orbit interactions were not included in SIESTA calculations. A value of 100 Ry was used as plane-wave cutoff for the grid.

The perovskite model system is made by 3×5×3 and 3×5×5 perovskite slabs orientated along the 110 direction for the MAI- and PbI_2-terminated surface, respectively. The 3×5×3 model is the same reported in a previous paper (Mosconi et al., 2016). Finally, we calculated the binding energies as the difference between the interacting Spiro-OMeTAD and O5H-OMeDPA (mol@$MAPbI_3$) and the single fragments (perovskite slab, $MaPbI_3$, and single molecules, mol) using the following formula:

$$\Delta E_{\text{binding}} = E_{\text{mol@MAPbI}_3} - E_{\text{mol}} - E_{\text{MAPbI}_3}.$$

SCLC Mobility Measurements: An indium-doped tin-oxide (ITO) coated glass substrate was patterned by laser etching. The substrate was carefully cleaned in ultrasonic baths of Hellmanex (2%, deionized water), deionized water, ethanol, and acetone, respectively. A 30-nm-thick, PEDOT:PSS layer was spin-coated onto the substrate, which was then annealed at 150 °C for 15 min in air. The 40 mM O5H-OMeDPA in chlorobenzene was spin-coated at 4000 rpm for 30 s to yield a flat thin film. An 80-nm-thick gold layer was then evaporated onto the active layer under high vacuum (<10^{-4} Pa). *J–V* curves were measured with a Keithley 2400 Source-Measure unit. The hole mobility was determined by fitting *J–V* curves with the equation

$$J = \frac{9}{8} \varepsilon_0 \varepsilon_r \mu \frac{V^2}{d^3}.$$

where ε_0 and ε_r is the vacuum and relative permittivity, respectively, and d is the hole-transporting layer thickness.

Deposition of Electron-Transporting Layer: An etched fluorine doped tin oxide (FTO) conducting glass was ultrasonically cleaned with Hellmanex (2%, deionized water), acetone, and ethanol in turn for 10 min. Afterwards the substrate was treated with UV-ozone for 20 min. A 30 nm TiO_2 blocking layer was then deposited by spray pyrolysis employing O_2 as the carrying gas at 450 °C from a precursor solution of 0.6 mL titanium diisopropoxide bis(acetylacetonate) and 0.4 mL acetylacetonate in 9 mL anhydrous ethanol. Next, a 200-nm-thick mesoporous TiO_2 layer was coated on the substrate by spin-coating for 20 s at 5000 rpm with a ramp rate of 2000 rpm s^{-1}, using the commercial TiO_2 paste (30NRD) diluted with anhydrous ethanol at a weight ratio of 1/6. After drying at 100 °C for 10 min, the TiO_2 film was annealed at 450 °C for 30 min under dry air flow to remove organic components.

Deposition of Triple Cation Perovskite Layer: Perovskite precursor solution contains 1.30 M PbI_2, 1.19 M FAI, 0.14 M $PbBr_2$, and 0.14 M MABr, dissolved in the DMSO/DMF (v/v, 1/4) mixture. 1.5 M CsI stock solution in DMSO was added into the perovskite precursor to obtain the desired triple cation composition $(FAPbI_3)_{0.85}$ $(MAPbBr_3)_{0.10}$ $(CsPbI_3)_{0.05}$ $(PbI_2)_{0.03}$. The perovskite film was deposited by a consecutive two-step spin-coating process at 2000 rpm for 10 s (ramp rate 200 rpm s^{-1}) and 6000 rpm for 30 s (ramp rate 2000 rpm s^{-1}) on the electron-transporting layer. At the time of 15 s prior to the program end, 100 μL of chlorobenzene was dripped on the spinning substrate, and the film was then annealed at 100 °C for 1 h. The preparation of the perovskite layer was carried out in a dry air filled glove box with a <2% relative humidity.

Deposition of Hole-Transporting Layer and Gold Electrode: 40 mM O5H-OMeDPA or 73 mM spiro-OMeTAD in chlorobenzene was spin-coated atop the annealed perovskite films at 4000 rpm for 20 s. The hole-transporters were doped with lithium bis(trifluoromethylsulfonyl)imide (Sigma-Aldrich) and 4-*tert*-butylpyridine (Sigma-Aldrich) in a molar ratio of 0.5 and 3.3, respectively. The hole-transporting layer was deposited in

a dry air filled glove box with a <2% relative humidity. Finally, an 80-nm-thick gold layer was thermally evaporated on top of the device.

***J–V* Characteristics:** *J–V* characteristics of PSCs were measured under simulated sunlight using a 450 W xenon lamp (Oriel, USA) equipped with a Schott K113 Tempax sunlight filter (Praezisions Glas and Optik GmbH). The data were recorded with a digital source meter (Keithley model 2400, USA). The light intensity was tested by a calibrated Si reference diode equipped with an infrared cutoff filter (KG-3, Schott) during each measurement. The photoactive area was 0.16 cm^2 using a non-reflective metal mask. The potential scan rate was 50 mV s^{-1} with a 5 mV voltage step. No preconditioning was performed before *J–V* measurement. Maximum power point (MPP) tracking measurements were performed with a Keithley model 2400 source meter driven by an algorithm implemented in the IgorPro software.

Photoluminescence Spectroscopy and Time Resolved PL Spectra: Steady-state PL and time-resolved PL measurement were performed with a LifeSpec-II fluorescence spectrometer.

IPCE Spectra: The IPCE system was equipped with a 300-W xenon lamp (ILC Technology) and a Gemini-180 double monochromator (Jobin Yvon Ltd). The IPCE spectra were recorded using a Model SR830 DSP Lock-In Amplifier (Stanford Research Systems).

Stability Measurements: The operational stability measurements were conducted by MPP tracking of PSCs under continuous illumination of a white 1 sun equivalent LED lamp with a Biologic SP 300 potentiostat. The MPP data were updated every 60 s using a standard perturb and observe method. A Peltier element was directly contacted with the device to precisely control the temperature of PSCs, and the temperature was recorded by a surface thermometer inserted between the Peltier element and PSCs. Before MPP tracking, the devices were stabilized through aging under one sun illumination for 20 min. The mask with 0.25 cm^2 aperture area was used on top of the cell.

Table S1. Synthetic Cost of One Gram of O5H-OMeDPA. Related to Figure 1A.

	Weight of reaction reagent [g]	Weight of reaction solvent [g]	Weight of workup solvent [g]	Price of chemical [USD/kg]	Chemical cost [USD]	Cost per step [USD]
[1,1'-binaphthalene]-2,2'-diol	1.183			336.44	0.398	
TsOH	0.711			24.30	0.017	
toluene		20	200	4.96	1.091	
silica-gel			20	5.41	0.108	
O5H						1.615
O5H	0.642			1615.00	1.037	
NBS				47.50	0.041	
DCM				1.57	0.031	
Br-O5H						1.108
Br-O5H	0.686			1108.00	0.760	
4,4'-dimethoxydiphenylamine	0.776			5521.13	4.284	
$Pd_2(dba)_3$	0.073			11800.00	0.861	
$P(t\text{-}Bu)_3 \cdot HBF_4$	0.047			2167.12	0.102	
$NaO(t\text{-}Bu)$	0.465			27.55	0.013	
silica-gel			2	5.43	0.011	
toluene		30	200	3.70	0.851	
alumina			50	11.92	0.596	
O5H-OMeDPA						7.478
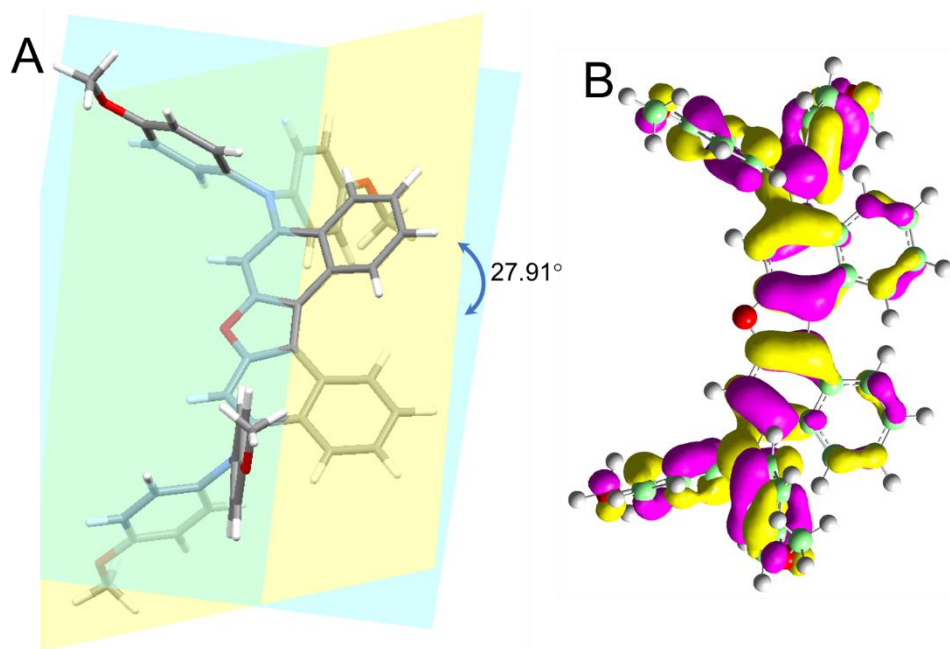
Figure S1. Geometry and HOMO Profile. Related to Figure 1.

(A) The DFT-optimized geometry of O5H-OMeDPA. The interplanar angle between two terminal benzene rings is 27.92°.

(B) HOMO distribution of O5H-OMeDPA based on the DFT-optimized geometry. The isodensity surface value is kept at 0.03.
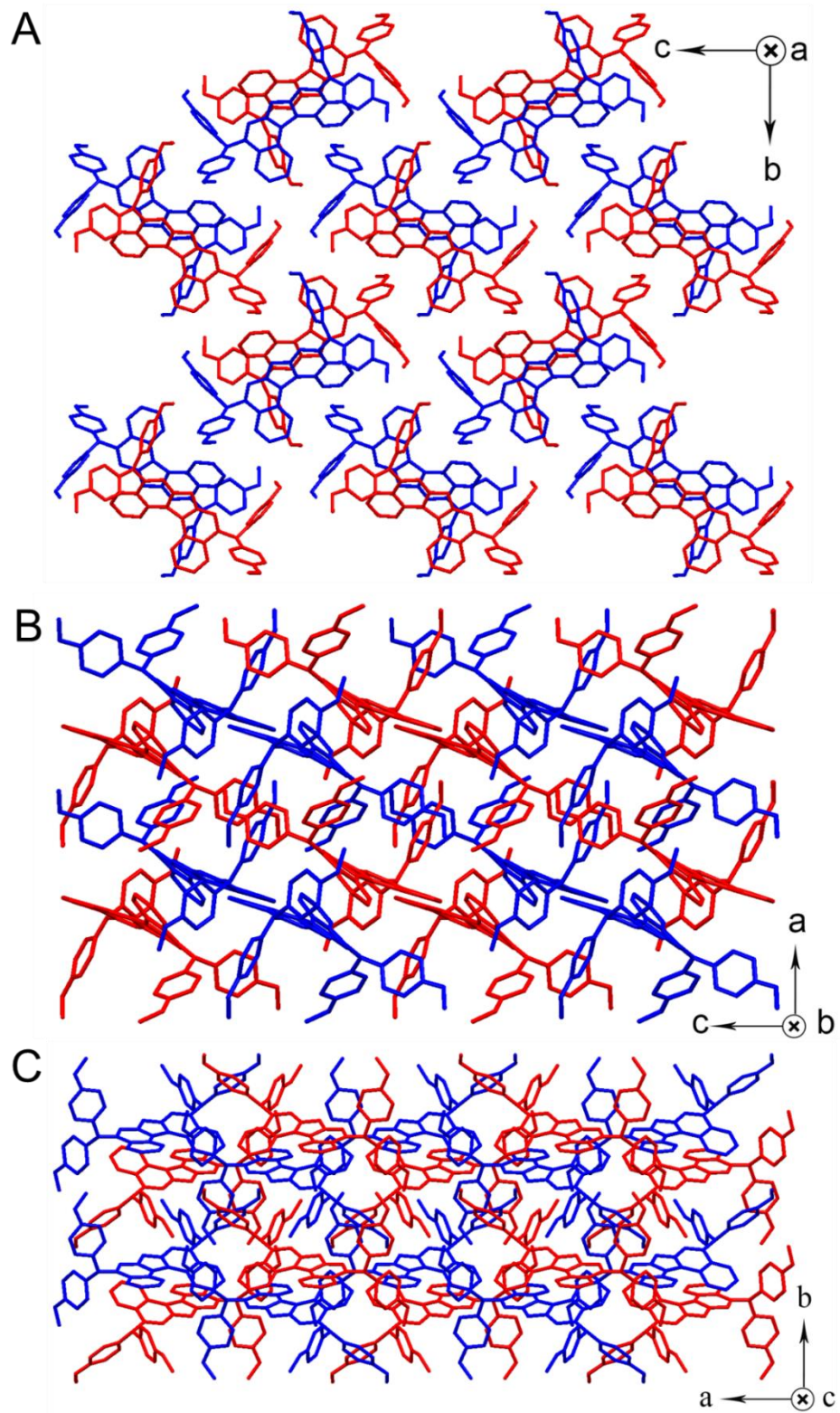
Figure S2. O5H-OMeDPA single crystal structures in a view along the crystallographic *a* axis (A), *b* axis (B), and *c* axis (C). Related to Figure 1.

Table S2. Crystal data and structure refinement for O5H-OMeDPA. Related to Figure 1.

Compound	O5H-OMeDPA
Empirical formula	$C_{48}H_{38}N_2O_5$
Formula weight	722.80
Temperature	170 K
Wavelength [Å]	0.71073
Crystal system	Monoclinic
Space group	P2(1)/c
a [Å]	10.0055 (2)
b [Å]	19.0313 (4)
c [Å]	19.3790 (4)
α [°]	90
β [°]	90.021 (1)
γ [°]	90
Volume [Å^3]	3690.10 (13)
Z	4
ρ_{calc}[g cm^{-3}]	1.301
μ [mm^{-1}]	0.084
F[000]	1520.0
Crystal size [mm^3]	0.36×0.35×0.30
2θ range for data collection [°]	2.30 to 25.31
Refl. collected	24108
Independent reflections	5491
Data/restraints/parameters	6750/0/500
Data completeness	0.997
Goodness-of-fit on F^2	1.045
Final R indexes [I>=2σ (I)]	R1=0.0401, wR2=0.0900
Final R indexes [all data]	R1=0.0529, wR2=0.0994
Largest diff. peak/hole [e Å^{-3}]	0.167/−0.194
CCDC deposition number	1885119
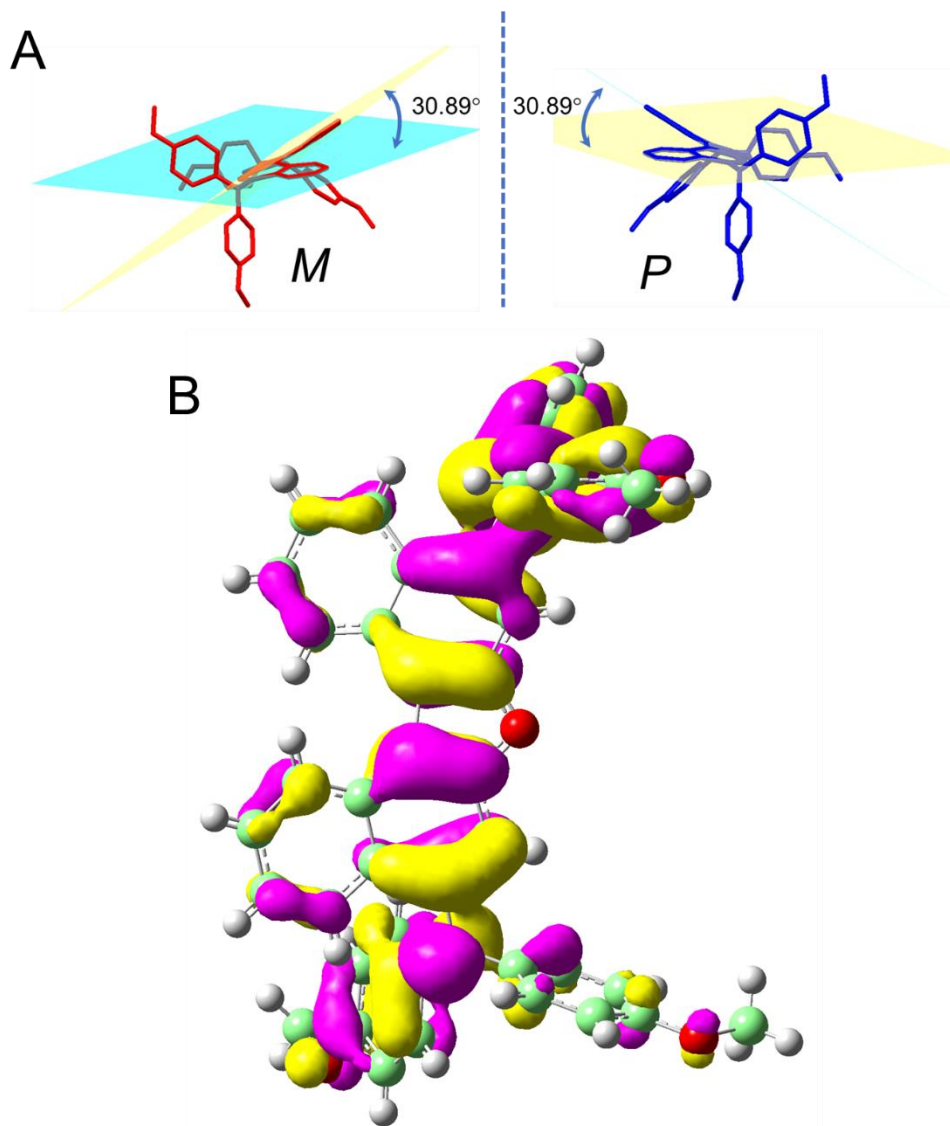
Figure S3. (A) Geometries of O5H-OMeDPA enantiomers extracted from single-crystal analysis. (B) HOMO distribution of O5H-OMeDPA based on the geometry extracted from single crystal analysis. Related to Figure 1. The isodensity surface value is kept at 0.03.
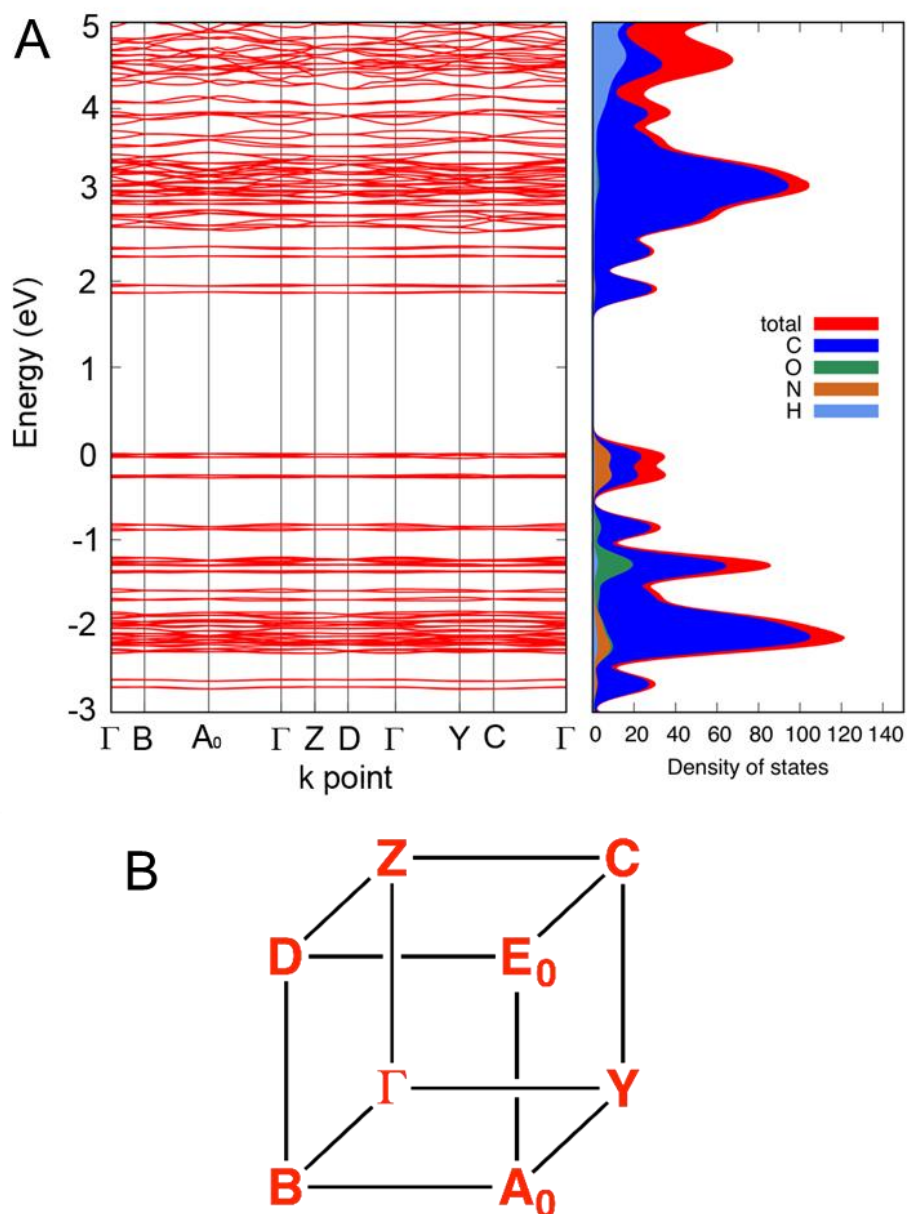
Figure S4. (A) Band structure (on the left) and projected density of states PDOS (on the right) of the O5H-OMeDPA single-crystal calculate at the DFT/GGA-PBE level of theory. (B) High symmetry points of P21/C space group in the first brillouin-zone. Related to Figure 1. In the band graphic, high symmetry points in the first Brillouin zone are labeled in crystallographic coordinates as follows: Γ) (0,0,0), B) (0,0,0.5), A_0) (0.5,0.0,0.5), Z) (0,0.5,0), D) (0,0.5,0.5), Y) (0.5,0,0) and C) (0.5,0.5,0). In the DOS graphic, the total density of states is reported in red, while the carbon, oxygen, nitrogen, and hydrogen contributions are signified in dark-blue, green, orange, and light-blue, respectively.
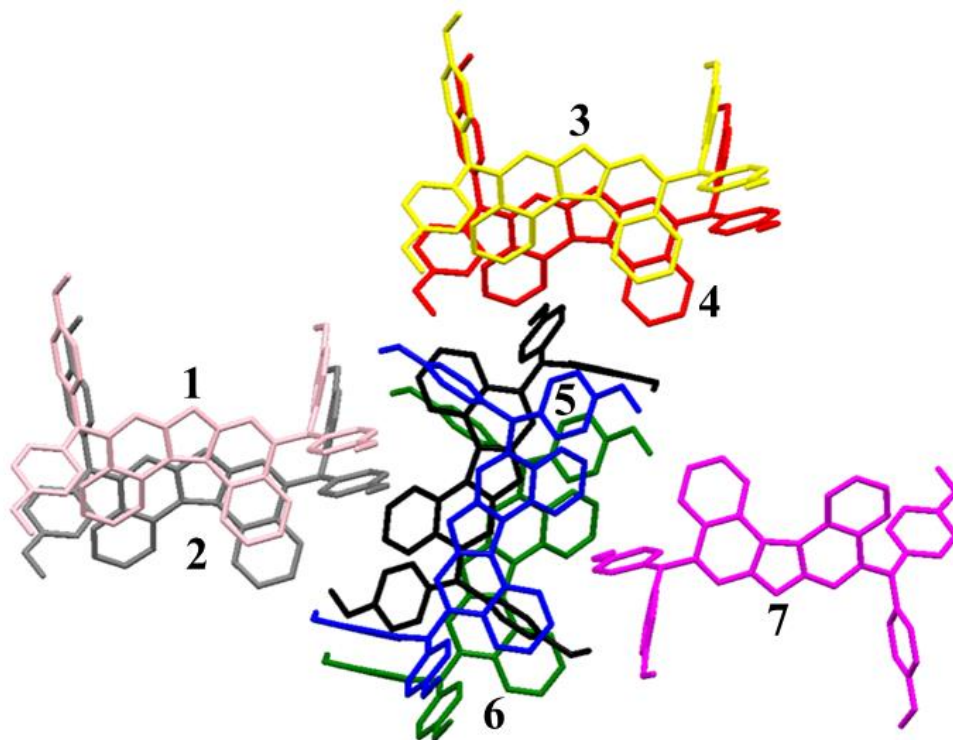
Figure S5. Main hopping paths in the O5H-OMeDPA single-crystal. Related to Figure 1.

The black molecule is selected as central hole donor.

Table S3. Center-of-mass distances, electron transfer integrals, and hole hoping rates of O5H-OMeDPA in single-crystal. Related to Figure 1.

λ [eV]	Path	Distance [Å]	V [meV]	k_i [s^{-1}]	μ [cm V^{-1} s^{-1}]
0.327	1 (pink)	13.194	4.69	2.69E10	0.047
	2 (grey)	13.016	6.28	4.82E10	
	3 (yellow)	16.509	4.69	2.69E10	
	4 (red)	13.016	6.27	4.80E10	
	5 (blue)	6.122	41.12	2.07E12	
	6 (green)	5.722	1.32	2.14E9	
	7 (magenta)	12.094	0.81	8.08E8	
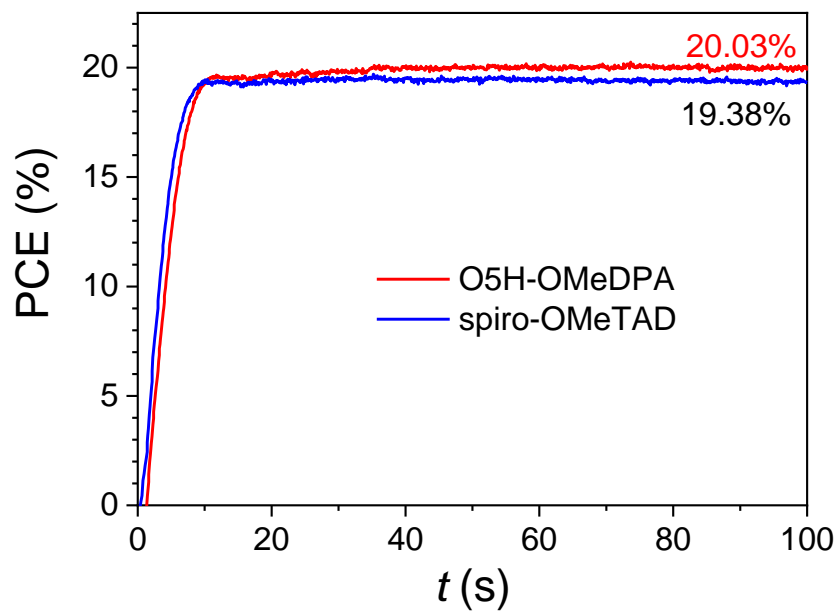
Figure S6. Maximum power point tracking of PSCs with O5H-OMeDPA and spiro-OMeTAD as the hole-transporting layers. Related to Figure 2.
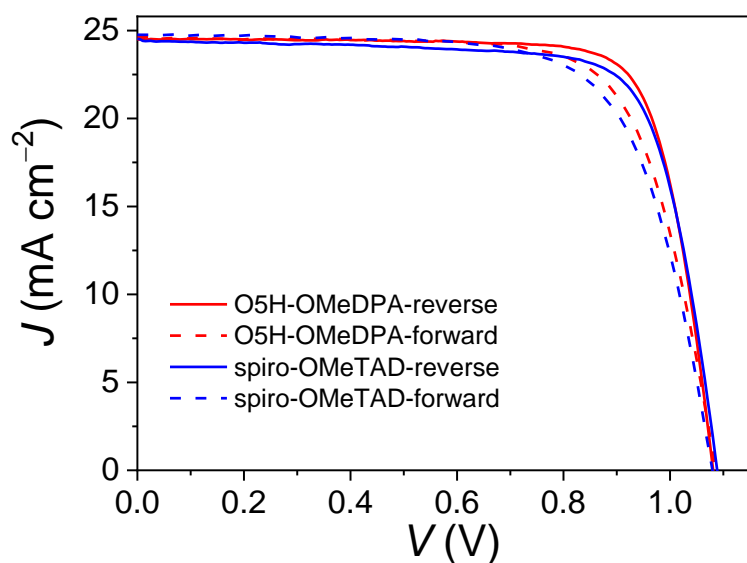
Figure S7. Forward and reverse *J–V* curves of the champion perovskite solar cells based on different hole transporters. Related to Figure 2. It is worth noting that the hysteresis index (HI) of devices are 7.5 % for O5H-OMeDPA, and 7.7% for spiro-OMeTAD, calculated from the equation $HI = \dfrac{PCE(reverse) - PCE(forward)}{PCE(reverse)}$. The similar HI values demonstrate that the hysteresis behavior is independent of HTLs. The hysteresis is likely related to the perovskite photoactive layer or the interface between the layers.
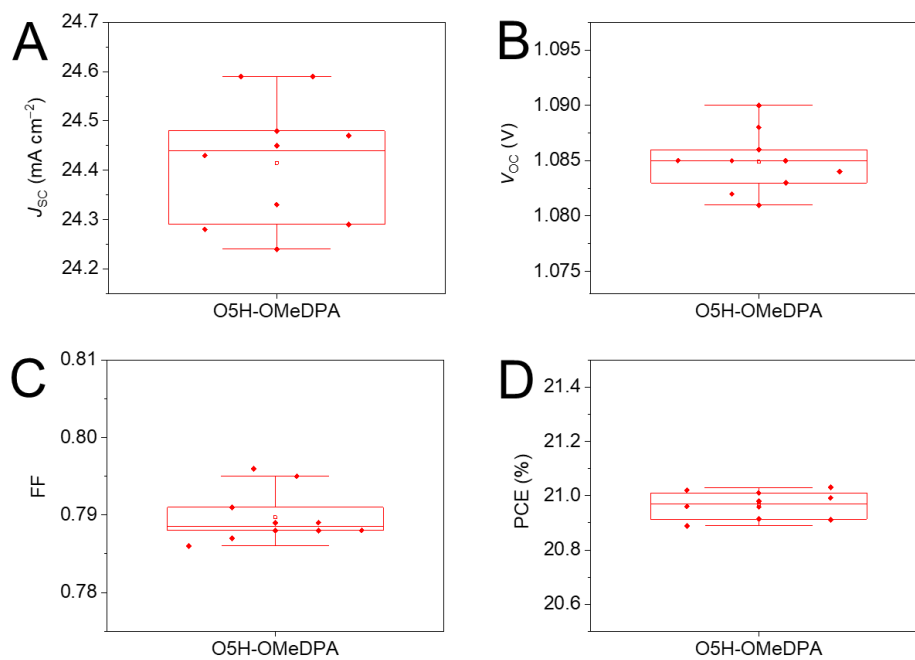
Figure S8. Photovoltaic metrics J_{sc} (A), V_{oc} (B), FF (C), and PCE (D) obtained from 10 devices with O5H-OMeDPA as the solution-processed hole-transporting layer. Related to Figure 2.
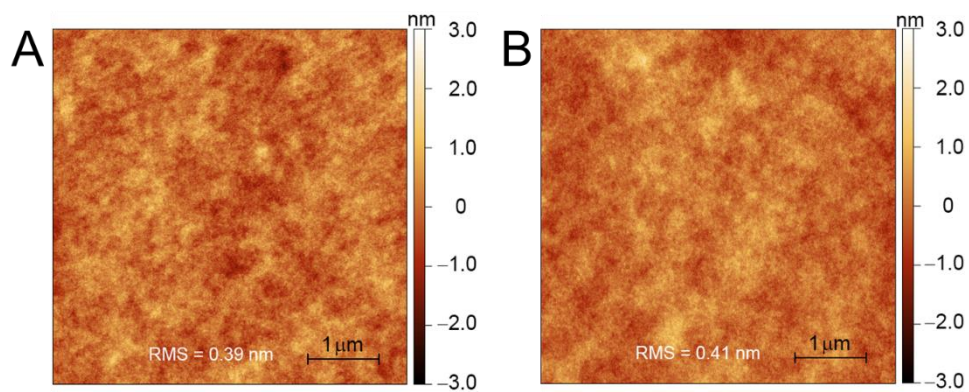
Figure S9. AFM images of O5H-OMeDPA (A) and spiro-OMeTAD (B) spin-coated on the substrates of PEDOT:PSS. Related to Figure 3.
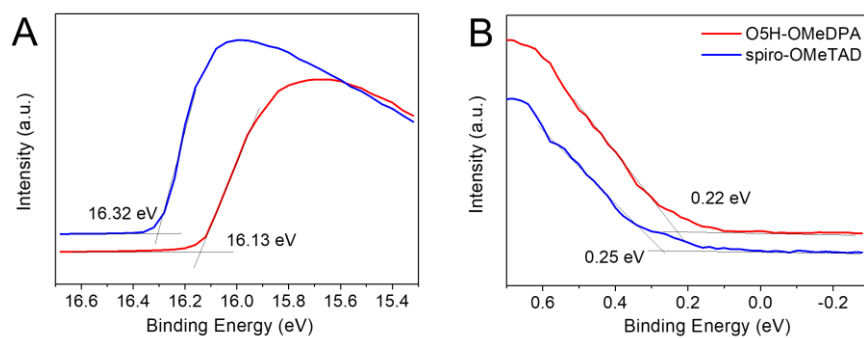
Figure S10. UPS spectra of O5H-OMeDPA and spiro-OMeTAD in the (A) cutoff and (B) onset energy regions. Related to Figure 3.
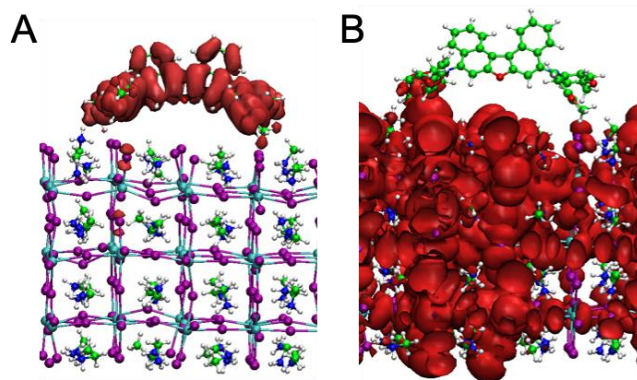
Figure S11. Inner HOMO orbital associated with O5H-OMeDPA (A) and inner valence band state of perovskite (B). Related to Figure 4.
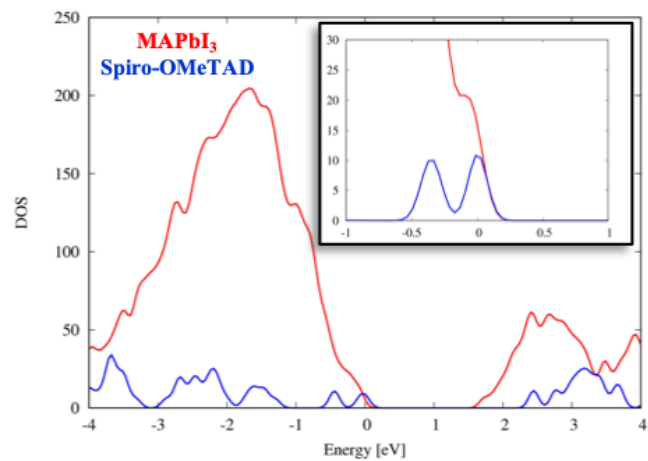
Figure S12. Projected density of states (PDOS) of spiro-OMeTAD adsorbed on the (110) surface of MAPbI$_3$. Related to Figure 4.
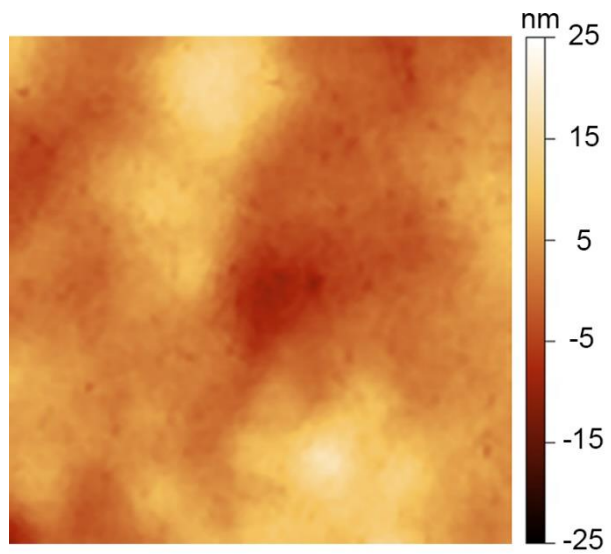
Figure S13. AFM image (1 μm × 1 μm) of the doped O5H-OMeDPA film spin-coated on the perovskite substrate after 12 h aging at 60 °C. Related to Figure 3.
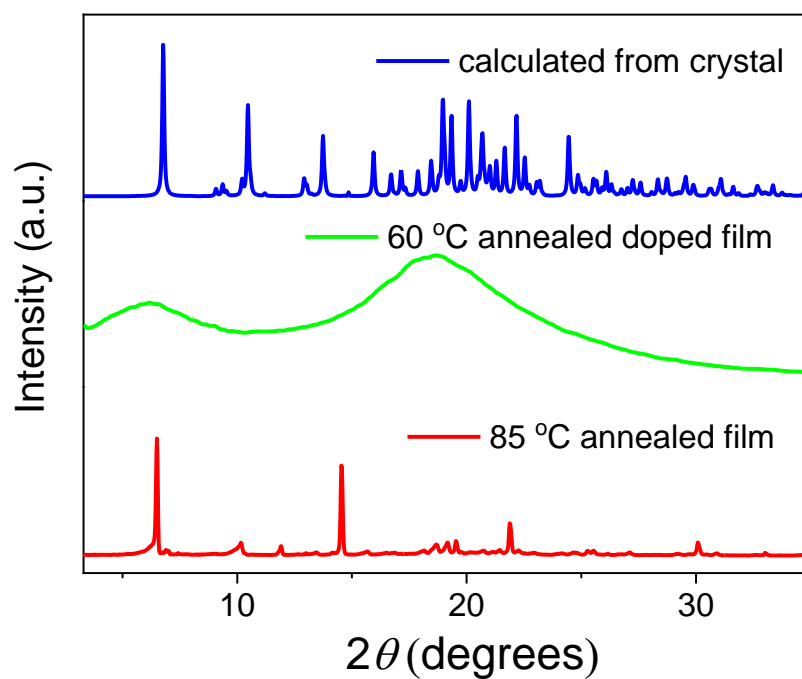
Figure S14. Experimental XRD patterns of the doped films aged at 60 °C for 12 h and dopant-free films aged at 85 °C for 12 h compared with the calculated XRD pattern using the single crystal parameters of O5H-OMeDPA. Related to Figure 4.
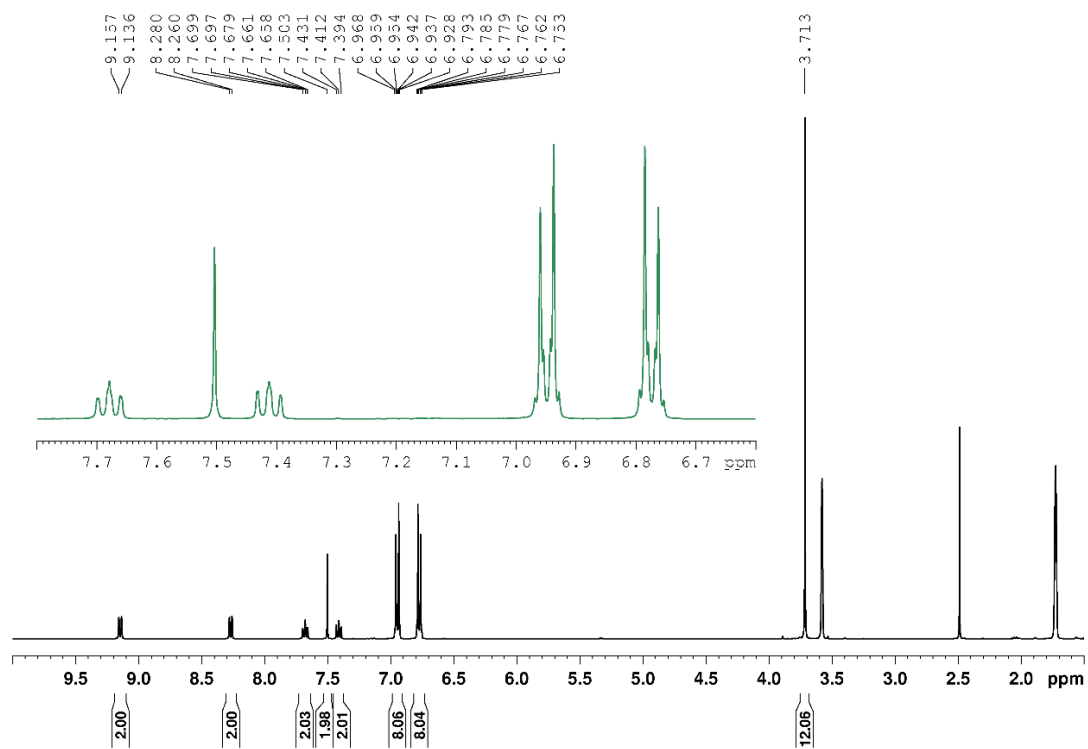
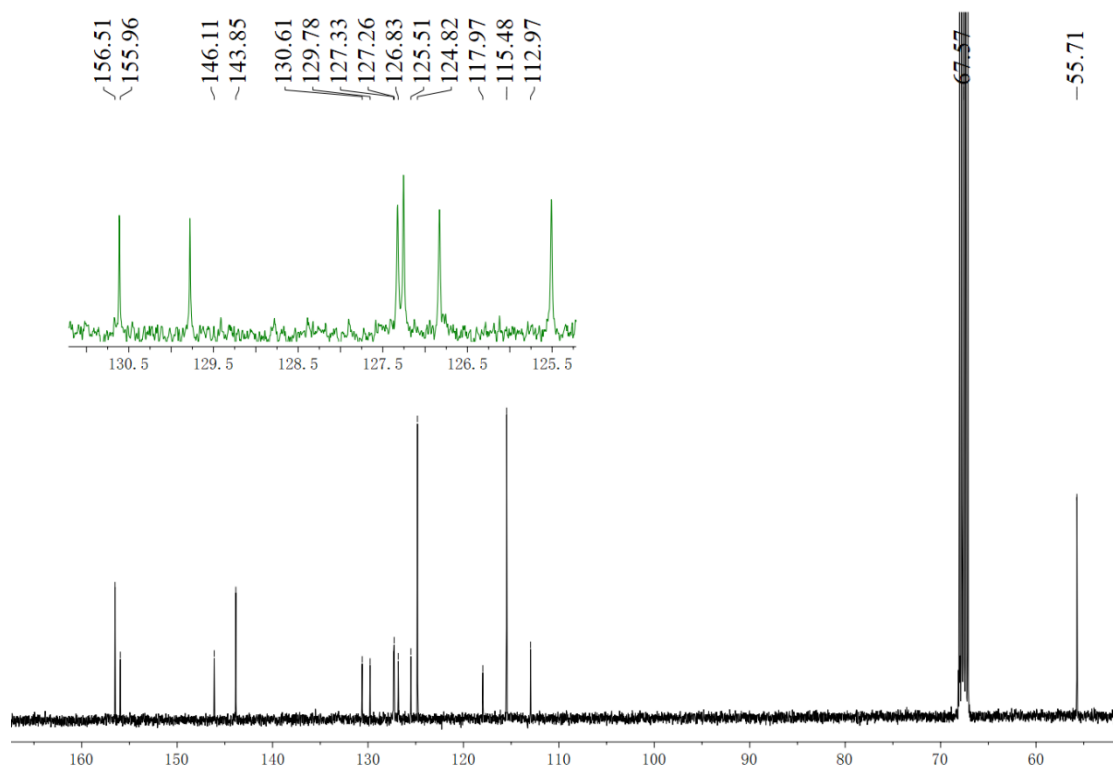**Figure S15.** ¹H NMR (400 MHz) spectrum of O5H-OMeDPA in THF-*d*₈. Related to Figure 1A.

Figure S16. ^{13}C NMR (101 MHz) spectrum of O5H-OMeDPA in THF-d_8. Related to Figure 1A.
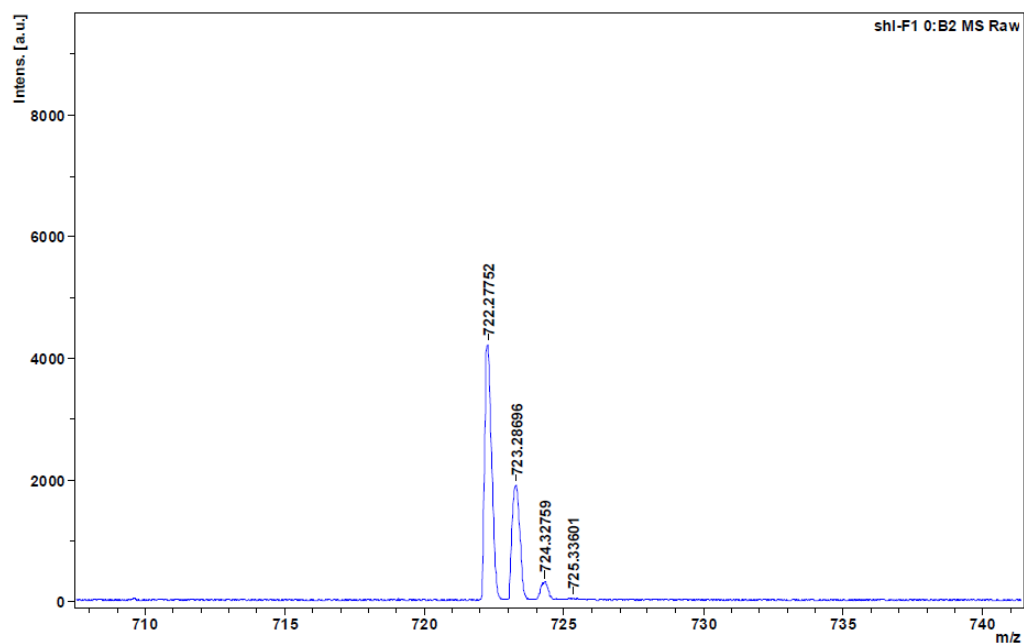
MALDI-TOF Mass Spectrum

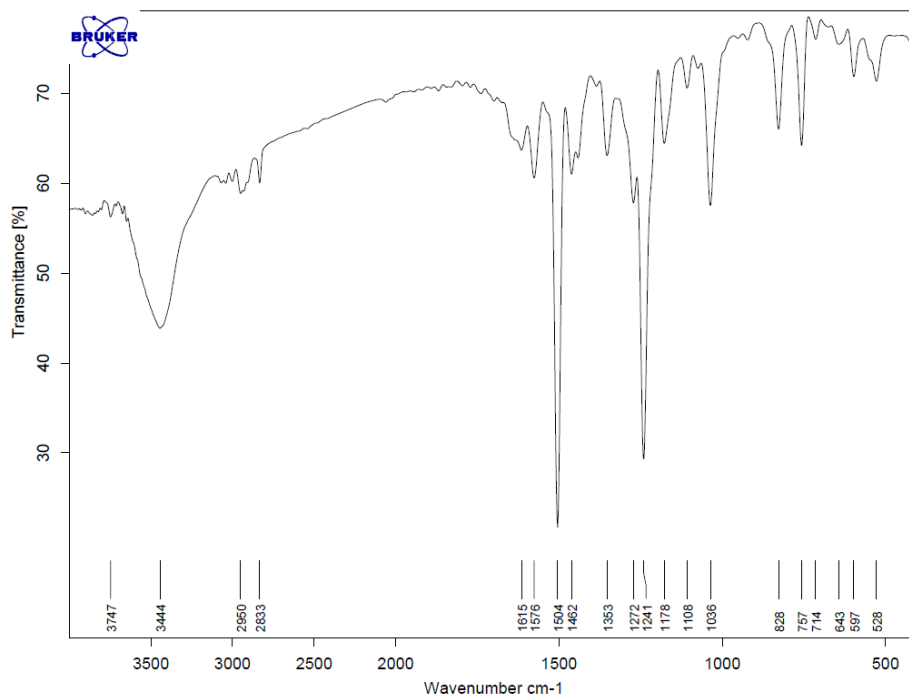Figure S17. High-resolution mass spectrum (MALDI-TOF) of O5H-OMeDPA. Related to Figure 1A.

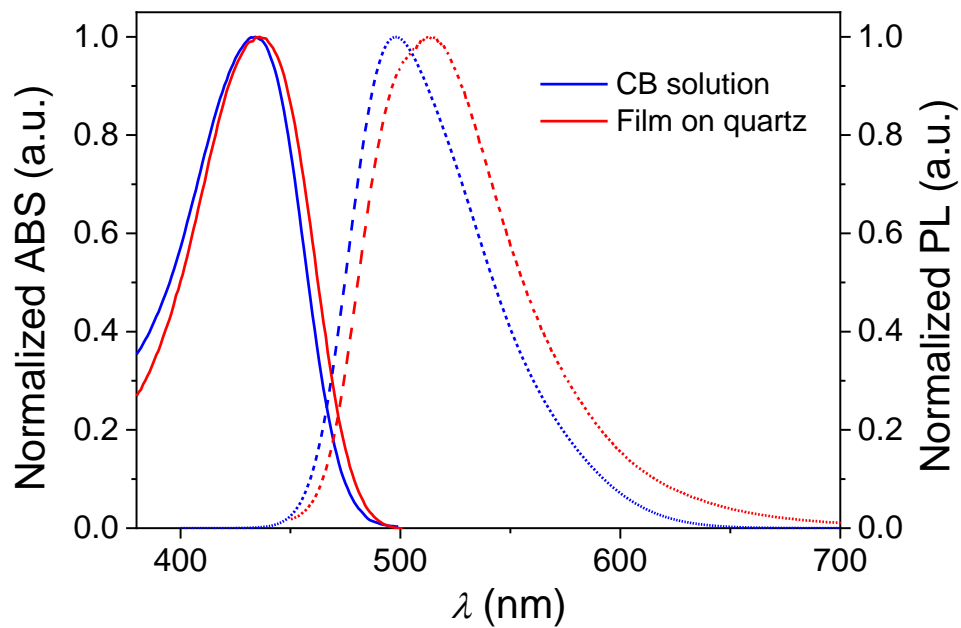**Figure S18. FTIR spectrum of O5H-OMeDPA. Related to Figure 1A.**

Figure S19. UV-vis absorption (solid line) and photoluminescence (dashed line) spectra of O5H-OMeDPA (15 μM) in chlorobenzene and its film spin-coated on quartz from chlorobenzene. Related to Figure 1A.

Supplemental References

Areephong, J., Ruangsupapichart, N., and Thongpanchang, T. (2004). A concise synthesis of functionalized 7-oxa-[5]-helicenes. Tetrahedron Lett. 45, 3067–3070.

Kunugi, Y., Maeda, A., Arakawa, T., and Okamoto, K. (2014). Fabrication of organic single crystal transistors based on 5,9-diphenyldinaphtho[2,1-*b*:1',2'-*d*]furan derivatives. J. Photopolym. Sci. Technol. 27, 317–320.

Giannozzi, P., Baroni, S., Bonini, N., Calandra, M., Car, R., Cavazzoni, C., Ceresoli, D., Chiarotti, G.L., Cococcioni, M., Dabo, I., Dal Corso, A., de Gironcoli, S., Fabris, S., Fratesi, G., Gebauer, R., Gerstmann, U., Gougoussis, C., Kokalj, A., Lazzeri, M., Martin-Samos, L., Marzari, N., Mauri, F., Mazzarello, R., Paolini, S., Pasquarello, A., Paulatto, L., Sbraccia, C., Scandolo, S., Sclauzero, G., Seitsonen, A.P., Smogunov, A., Umari, P., and Wentzcovitch, R.M. (2009). QUANTUM ESPRESSO: a modular and open-source software project for quantum simulations of materials. J. Phys.: Condens. Matter 21, 395502.

Perdew, J.P., Burke, K., and Ernzerhof, M. (1996). Generalized gradient approximation made simple. Phys. Rev. Lett. 77, 3865–3868.

Laasonen, K., Car, R., Lee, C., and Vanderbilt, D. (1991). Implementation of ultrasoft pseudopotentials in *ab initio* molecular dynamics. Phys. Rev. B 43, 6796–6799.

Soler, J.M., Artacho, E., Gale, J.D., García, A., Junquera, J., Ordejón, P., and Sánchez-Portal, D. (2002). The SIESTA method for *ab initio* order-*N* materials simulation. J. Phys.: Condens. Matter 14, 2745–2779.

Wu, Z., and Cohen, R.E. (2006). More accurate generalized gradient approximation for solids. Phys. Rev. B 73, 235116.

Mosconi, E., Grancini, G., Roldán-Carmona, C., Gratia, P., Zimmermann, I., Nazeeruddin, M.K., and De Angelis, F. (2016). Enhanced TiO_2/$MAPbI_3$ electronic coupling by interface modification with PbI_2. Chem. Mater. 28, 3612–3615.